ADVANCED FUNCTIONAL MATERIALS
www.afm-journal.de

Understanding and Optimizing Li Substitution in P2-Type Sodium Layered Oxides for Sodium-Ion Batteries

*Mingfeng Xu, Giovanni Gammaitoni, Michael Häfner, Eduardo Villalobos-Portillo, Carlo Marini, and Matteo Bianchini**

In the quest to improve cathode materials for Na-ion batteries, a family of Li-substituted P2 layered oxides with nominal stoichiometry $Na_{5/6}Li_yNi_{5/12-3y/2}Mn_{7/12+y/2}O_2$ ($y = 2/18, 3/18, 4/18, 5/18$) is studied. The consequences of Li substitution and the challenge of elevating the Na content are explored. Structurally, honeycomb ordering is observed in all samples, while Li induces the loss of Na^+/vacancy ordering. Electrochemically, the materials exhibit an increasing trend of polarized hysteresis in the 1st cycle. Semi-simultaneous *operando* x-ray absorption and diffraction are coupled to appreciate the structural evolution and redox behavior during this process. Li in the transition metal site eliminates phase transitions at high voltage and modifies the activation of O-redox. All samples show anionic redox: as confirmed computationally, in the Li-free sample this is rooted in Ni—O hybridized states, while in the Li-containing samples in O non-bonding states. Composition $Na_{0.745(6)}Li_{0.164(4)}Ni_{0.238(1)}Mn_{0.599(3)}O_2$ proves to have the least O-redox among all, coupled with reduced phase transitions, disordered occupancy of Na sites, and small volume change during cycling, leading to the best balance of cycling stability (≈92% after 100 cycles), capacity (> 100 mAh g^{-1}) and rate capability. This can pave the way for further development of P2 layered oxides with redox-inactive dopants.

1. Introduction

Sodium ion batteries are promising alternatives to complement lithium ion batteries in the modern energy storage market.[1,2] The similarities between the intercalation chemistries of Na and Li have accelerated the quest for energy-dense Na-ion battery electrode materials during the last decade.[3] Among sodium-based cathodes, layered oxides (Na_xTMO_2, TM = transition metal) are one of the most attractive candidates. These materials tend to form into two main polytype structures, as distinguished by the Na environments: P-type structures accommodate Na within prismatic sites between neighboring TMO_2 layers, whereas O-type ones exhibit octahedrally coordinated Na. According to the oxygen stacking sequence, they are further categorized into P2, O3, P3, etc., where the number indicates a two- or three-layer stacking sequence of oxygen.[4,5]

In the Na_xTMO_2 system, P2 and O3 are two of the most studied structures. In regard to Na^+ conductivity, P2 is believed to be preferable over O3 as it offers open prismatic pathways with a lower energy barrier for Na diffusion, at least for a large portion of the x domain.[6] P2-type $Na_{2/3}Ni_{1/3}Mn_{2/3}O_2$ is considered a prototypical P2 material, able to deliver a high specific capacity at high operating voltage based theoretically on Ni-redox.[7–9] With the redox couple of $Ni^{2+/4+}$ and potentially $O^{2-/n-}$, a Ni-containing P2 material might also allow easy handling due to its relatively good air-stability.[10] An issue for all P2 materials is the fact that they are typically synthesized at low Na content, i.e., often close to $x = 2/3$, and can rarely reach beyond 3/4, which is problematic when building full cells.[11–13] The major drawback, however, is the P2–O2 phase transition occurring at high voltage during electrochemical cycling, typically when $x < 1/3$, which is not well reversible due to the large volume variation involved, and which limits cycling stability and capacity retention.[7,14,15] Elemental substitution with redox-inactive elements such as Li^+, Mg^{2+} or Al^{3+} has been reported to effectively mitigate this structural variation, yet at the expense of a lower available specific capacity.[16–18]

Despite the fact that some of these lithium substitutions have been already reported, it is to date unclear what the optimum amount would be. The reason for this is that increasing substitution leads to a lower amount of available transition metals redox activity, yet oxygen redox activity has been widely reported for such compounds, extending the range of options available for materials design.[19–23] We focus here on maximizing the Na

M. Xu, G. Gammaitoni, M. Häfner, M. Bianchini
Faculty of Biology
Chemistry and Earth Sciences
University of Bayreuth
Universitätstraße 30, 95447 Bayreuth, Germany
E-mail: matteo.bianchini@uni-bayreuth.de
M. Xu, G. Gammaitoni, M. Häfner, M. Bianchini
Bavarian Center of Battery Technology (BayBatt)
Weiherstraße 26, 95448 Bayreuth, Germany
E. Villalobos-Portillo, C. Marini
ALBA Synchrotron
Cerdanyola del Vallès, Barcelona 08290, Spain
The ORCID identification number(s) for the author(s) of this article can be found under https://doi.org/10.1002/adfm.202425499

DOI: 10.1002/adfm.202425499

content in the P2 structure, and as dopant on the lightest available inactive element, Li, synthesizing systematically a family of Li-substituted P2 layered oxides, with nominal stoichiometry of $Na_{5/6}Li_yNi_{5/12-3y/2}Mn_{7/12+y/2}O_2$. The Li content y was designed to increase stepwise (2/18, 3/18, 4/18, 5/18), to investigate its role of stabilizing the P2 structure over cycling. Accordingly, the Ni concentration decreases and Mn increases, assuming always the presence of Mn^{4+} in our samples. We expect the Ni-redox activity to decrease with y, and possibly the O-redox activity to increase accordingly. The synthesized samples are labelled as LNM-2, LNM-3, LNM-4, and LM, respectively. We also prepared the prototypical $Na_{2/3}Ni_{1/3}Mn_{2/3}O_2$ as a reference material, and it is labelled as NM. Although there have been previous studies focusing on achieving a higher Na level in the Ni-/Mn-/Li-based P2 materials, our study differs from these as it does not focus on a single material but rather on a family of compounds, and moreover in the fact that we show P2 phases only, without O3 ones, which can be often observed in the literature by the presence of side reflections next to the main 002 one.[24–26]

After verifying the crystal structure, cationic orderings and the electrochemical performances of the materials, we then address the charge compensation mechanism of such compounds by combining semi-simultaneous *operando* synchrotron x-ray diffraction (XRD) and x-ray absorption near edge structure (XANES) during the first charge/discharge cycle. *Operando* XRD reveals the evolution of the crystal structure of the compounds, showing that structural pathways changed over cycling with different Li concentrations. Meanwhile, the *operando* XANES on Ni and Mn K-edge indicated the transition metal behavior and, indirectly, the oxygen contribution over cycling. Via this strategy of combined *operando* techniques, we are able to suggest at which point during the first cycle the oxygen activity starts to take place, and how much capacity it contributes. The results are further corroborated by ex situ EXAFS (extended x-ray absorption fine structure) and SEM-EDX (scanning electron microscopy - energy-dispersive x-ray spectroscopy), as well as by density of states computed by Density Functional Theory (DFT). By combining this information with the amount of structural stabilization observed (avoided phase transitions and volume change at the top of charge), we can identify the compound structurally and electrochemically more promising for further research and practical applications.

2. Results and Discussion

2.1. Design Principle

The Na content is a key aspect of applying layered oxides as positive electrode materials. The ultimate expectation is to use them in full cells where the Na supply is limited. In their pristine state, P2 materials typically have a Na content of 0.67 (or 2/3) per formula unit, while it usually exceeds 0.9 in O3 compounds.[11,12] This motivated us to achieve a higher Na reservoir in a P2 system, from the regular 2/3 to 5/6 while preserving the P2 structure. A challenge is the unfavorable simultaneous occupation of the nearest-neighboring prismatic Na sites. In most literature reports, a high Na content over 0.8 could already induce the formation of O3.[11,12] To predict the tendency of a compound to crystallize into P2 or O3 polymorphs, Zhao et al. mapped the weighted

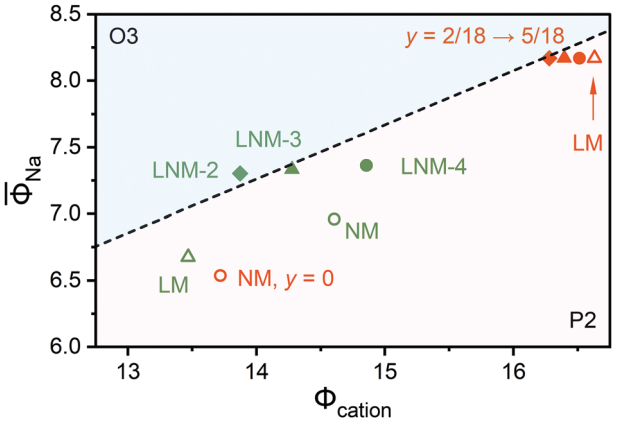

Figure 1. Compositions of the targeted layered oxides (orange symbols) $Na_{5/6}Li_yNi_{5/12-3y/2}Mn_{7/12+y/2}O_2$ (y = 2/18, 3/18, 4/18, 5/18) and $Na_{2/3}Ni_{1/3}Mn_{2/3}O_2$, according to average Na ionic and cationic potential. The actual synthesized compounds based on the refined compositions are also shown (green symbols), correspondingly using the same shape as the target ones. The end members NM and LM are shown with empty symbols, the intermediate compounds (LNM-2, LNM-3, and LNM-4) with filled symbols.

average Na ionic potential $\overline{\Phi_{Na}}$ versus the overall cationic potential Φ_{cation}, observing a clear boundary between the two phases (**Figure 1**).[27] The weighted average ionic potential of a single ion is given by the ratio of its charge number to the radius; the overall cationic potential is normalized dividing by the ionic potential of O^{2-}.[27] Following this prediction, we designed our compositions by tuning the TM stoichiometry. We considered charge balance based on the oxidation state of Ni and Mn being 2+ and 4+, respectively. Our target compositions with stoichiometry $Na_{5/6}Li_yNi_{5/12-3y/2}Mn_{7/12+y/2}O_2$ (y = 2/18, 3/18, 4/18, 5/18, (Figure 1, orange symbols)), are therefore positioned right below the boundary with a high $\overline{\Phi_{Na}} = 8.17$. They move toward the O3 region with a decreasing amount of Li (from the empty triangle to the filled diamond symbol). The reference compound of $Na_{2/3}Ni_{1/3}Mn_{2/3}O_2$ is in the lower left part of the plot ($\overline{\Phi_{Na}}$= 6.54). The member with nominal Li content of 1/18 was not successfully synthesized due to the significant intergrowth of other impurities, including the O3 phase. This is expected since indeed LNM-2 already falls around the boundary between P2 and O3, which further attests to the predictive ability of the ionic potential method.[27] Figure 1 (green symbols) also reports the actual compositions we obtained after structural characterization of the synthesized compounds, as we discuss in the following.

2.2. Structural and Morphological Characterization

Morphological characterization by SEM and EDX mapping for LNM-2 as an exemplary sample are shown in **Figure 2a**. One can notice the size of most particles ranges between 2 and 3 µm. The primary particles are roughly of hexagonal shape, consistent with the Bravais lattice symmetry. These primary particles are found to agglomerate into secondary particles of size reaching 20–30 µm. EDX mappings (Figure 2a) indicate that Na, TMs, and O are homogeneously distributed in the particle. The amount of Mn and Ni were in particular determined carefully as listed in Table S1

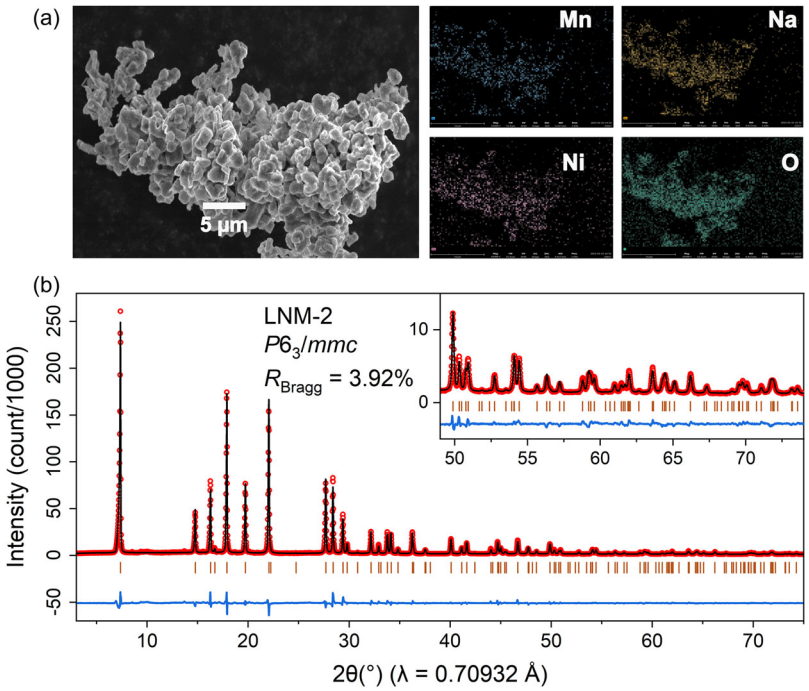

Figure 2. a) SEM image and EDX mapping of LNM-2 as an example for all tested P2-type samples. b) Rietveld refinement of powder XRD patterns of LNM-2. Red circles are experimental data points; black lines are refined patterns; brown bars are reference reflections of P2 ($P6_3/mmc$); blue lines are deviations between simulated and observed patterns.

(Supporting Information), demonstrating that the obtained ratio was very close to the target one.

Figure 2b and Figure S1 (Supporting Information) present the x-ray diffraction patterns of all samples, followed by the structural parameters obtained by Rietveld refinement in **Table** 1 and Tables S2–S5 (Supporting Information). The reflections can be indexed in two hexagonal space groups: $P6_3/mmc$ or $P6_322$, whose unit cells are displayed in Figure S2 (Supporting Information). Here, both space groups are used for refinement, and we discuss in the following the applicability of the simpler and widely adopted $P6_3/mmc$ model, followed by our reasons and findings regarding $P6_322$ with a larger unit cell.

At first the common model based on the hexagonal crystal system $P6_3/mmc$ was refined against the x-ray diffraction data of all samples under the following constraints: i) the sum of elements on TM site (Wyckoff 2*a* site) per formula unit equals 1; ii) the value of Ni:Mn was fixed to the one determined by EDX analysis. It was thus possible to determine the elemental distribution in the transition metal site, as well as the amount of Na in the Na sites (Wyckoff sites 2*b* and 2*d* whose occupancy is freely refined). The site occupancy results for the transition metals and Li do not deviate significantly from those expected (Table S1, Supporting Information). The Na content is found to be lower than expected, as we discuss in detail the following. The XRD data and their refinement also indicate the presence of a Li_2MnO_3 impurity (Tables S2–S5, Supporting Information). For all samples, the main P2 phase comprises at least 95 wt.% of the total, while the Li_2MnO_3 impurity increases with increasing Li content

Table 1. Exemplary Rietveld Refinement results of a $P6_3/mmc$ structural model against powder XRD data of LNM-2.

$Na_{0.745(6)}Li_{0.164(4)}Ni_{0.238(1)}Mn_{0.599(3)}O_2$				$P6_3/mmc$, $Z = 2$		
$a = b = 2.89005(2)$ Å				$R_{Bragg} = 3.92\%$		
$c = 11.02821(9)$ Å				$R_{wp} = 11.5\%$		
$V = 79.771(1)$ Å^3				$\chi^2 = 31.3$		
Atom	Wyck. sites	*x/a*	*y/b*	*z/c*	B_{iso}	Occ.
O	4*f*	1/3	2/3	0.0939(1)	1.09(5)	1.000
Li	2*a*	0	0	0	0.234(8)	0.164(4)
Ni	2*a*	0	0	0	0.234(8)	0.238(1)
Mn	2*a*	0	0	0	0.234(8)	0.599(3)
Na_f	2*b*	0	0	1/4	5.0(3)	0.272(4)
Na_e	2*d*	1/3	1/3	3/4	2.4(1)	0.473(4)

*constraints: Li+Ni+Mn = 1; Ni:Mn fixed to EDX value (Table S1, Supporting Information).

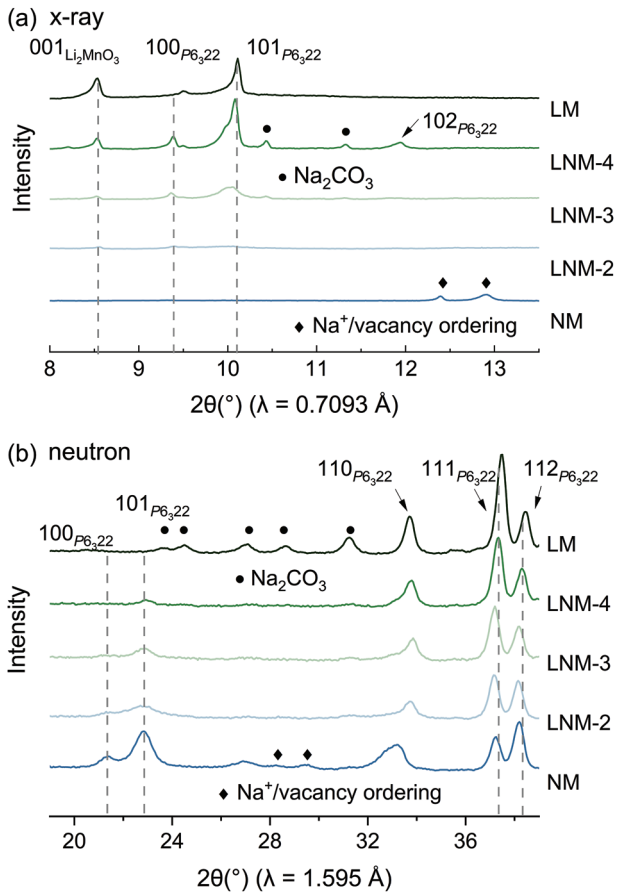

Figure 3. a) Zoomed-in XRD patterns of all samples from $2\theta = 8.0°$ to 13.5°. b) Zoomed-in ND patterns of all samples from $2\theta = 19.0°$ to 39°. The diamond symbols indicate the Na^+/vacancy ordering which disappears upon Li substitution. The circles indicate trace amount of Na_2CO_3 as an impurity.

from 0.81(8) wt.% (LNM-3) to 5.0(1) wt.% in LM (Tables S3a, S4a, and S5a, Supporting Information).

While $P6_3/mmc$ is useful to provide a global description of the P2 structures, we notice it cannot index several less-intense reflections, particularly in the 2θ range 8.0° to 13.5°, which are shown in Figure 3a. These have been reported to be related to superstructures caused either by transition metal ordering or by Na^+/vacancy ordering.[8,15,28–32] Specifically, the two relatively pronounced reflections at $\approx 2\theta = 9.4°$ and 10.1° are indication of a transition metal honeycomb superstructure.[8,9,29] A larger hexagonal unit cell with space group $P6_3$ ($a = \sqrt{3}a' = 5$ Å, $V = 3V'$, the primed being parameters with $P6_3/mmc$) was originally proposed by Lu et al. to index the additional reflections.[8] An alternative space group, $P6_322$, with the same unit cell size was also proposed to understand the superstructure peaks in P2 materials.[33,34] We compare the unit cell size of both space groups in Figure S2 (Supporting Information), while the structures can be seen also in **Figure** 4a–c.

From Figure 3a, it may appear that the honeycomb ordering is only present in the samples containing a large amount of Li. However, this is not surprising, since Li/Mn have strong contrast with x-rays, while a Ni/Mn ordering would be virtually invisible. Therefore, given the importance of cationic orderings in determining the properties of layered oxides,[8,35] we further used neutron diffraction (ND) to confirm their existence in our Ni-rich samples, as shown in Figure 3b. Here, the peaks related to honeycomb ordering can be clearly seen in NM between 21° and 24°. In Figure S3 (Supporting Information), we present an exemplary refinement of ND data for the NM sample (exact $Ni_{1/3}Mn_{2/3}$ ratio). Ni and Mn have scattering lengths of opposite signs (b_{Ni} = 10.3 fm, b_{Mn} = -3.73 fm, b_{Li} = -1.9 fm), therefore any ordering would be strongly apparent using neutrons. Indeed, we note that a small $P6_3/mmc$ unit cell is not satisfactory to explain many reflections which however can be indexed by the larger unit cells of space groups $P6_3$ or $P6_322$. These two space groups have the same extinctions, hence cannot be distinguished by powder diffraction data alone. We compared the refinements in both space groups in Figure S3 and Table S6 (Supporting Information). We note that $P6_322$ is preferable due to several reasons: i) $P6_322$ has higher symmetry; ii) it leads to slightly better quality of fit despite having fewer parameters; iii) $P6_322$ contains only one O position versus two in $P6_3$, which are always problematic during refinement and needs to be constrained; iv) Debye-Waller factors of Na are smaller; v) it also contains only three Na sites (**Table** 2) instead of four. This makes chemical sense as we discuss below.

We therefore settled to continue with the space group $P6_322$ also to refine all XRD patterns including superstructure peaks. In Figure S1 (Supporting Information), we compare the refinements of all samples with space groups $P6_3/mmc$ and $P6_322$ (left and right, respectively). As displayed in the enlarged region, the $P6_322$ model does improve the fitting at $\approx 2\theta = 9.4°$ and 10.1° for samples LNM-3, LNM-4 and LM. We then are able to index these two reflections to be 100_{P6322} and 101_{P6322}. However, as known for Li_2MnO_3 and Li_2NiO_3, these reflections are broadening asymmetrically by stacking faults, hence the fit is not perfect.[36,37] The question remains regarding LNM-2, where no superstructure peaks can be seen with x-rays. Here the refinement appears nearly perfect also using $P6_3/mmc$. However, once again using ND we can demonstrate that a honeycomb ordering still exists in LNM-2, as marked by grey dashed lines in Figure 3b. The same applies for LNM-3. The ND data and the related refinement can be found in Figure S4 (Supporting Information) and Tables S6–S10 (Supporting Information). It is therefore clear that all our samples possess honeycomb ordering superstructures in the TM planes, which become visible depending on the probe chosen for the diffraction experiment.

Considering now Figure 3 again, we note that there is another set of reflections near $2\theta = 12.5°$ and 13.0° in the non-lithiated sample NM. These two characteristic peaks were previously observed and attributed to Na^+/vacancy ordering requiring an even larger supercell to be fully described.[15,29–31] These peaks are however missing in all lithiated samples, indicating that Li substitution does disrupt the Na^+/vacancy ordering in the alkali layer. In conclusion, we can clearly state that the honeycomb ordering is present in all our samples, even though the Li substitution weakens the related reflections due to the increased site disorder. On the other hand, Na^+/vacancy ordering is disrupted when deviating from the exact $Ni_{1/3}Mn_{2/3}$ composition.

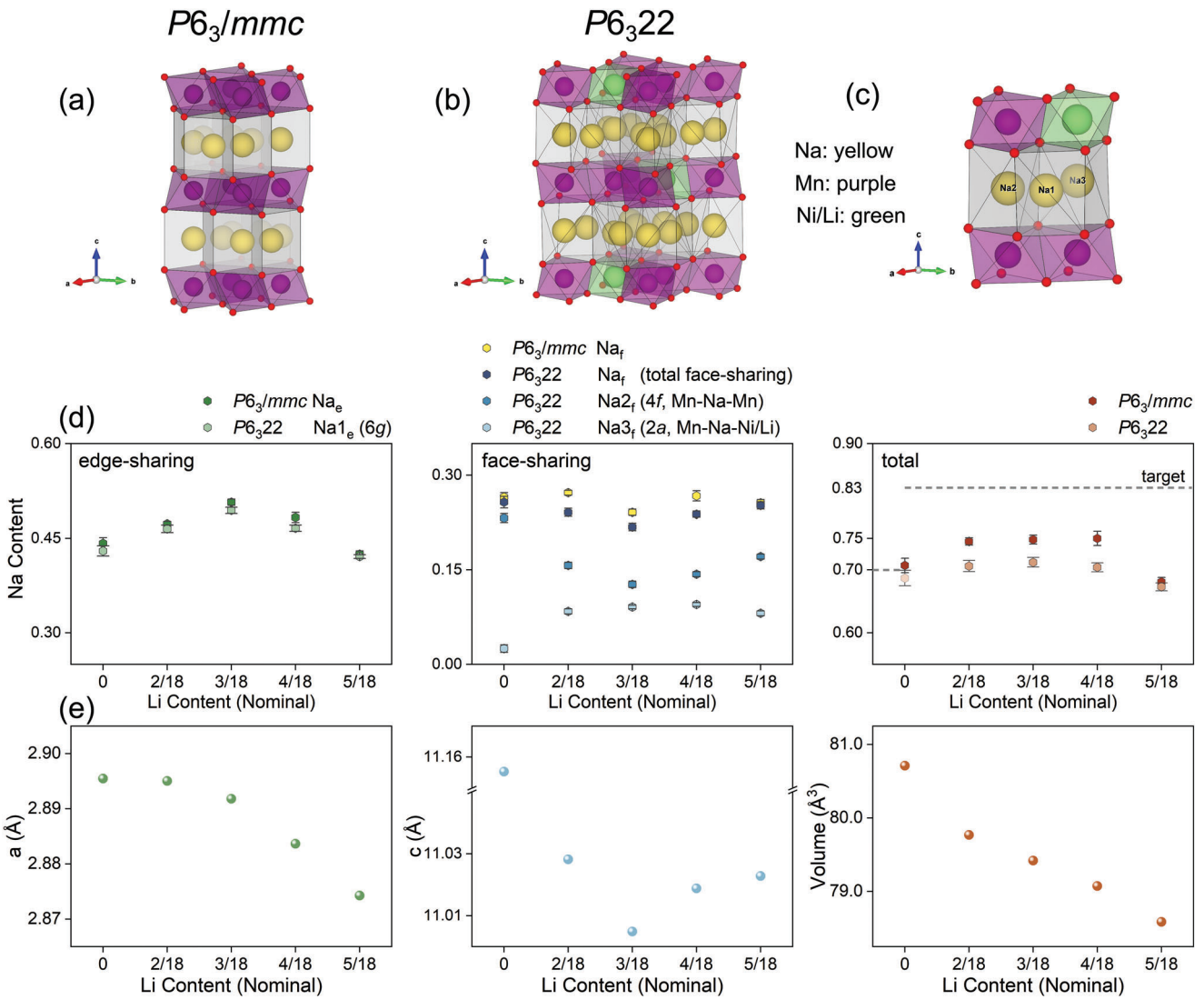

Figure 4. P2 structure displayed using the space group $P6_3/mmc$ a) and $P6_322$ b). A part of the $P6_322$ unit cell indicating the 3 types of Na atoms. c) Na1 is in 6*g* Wyckoff position (edge-sharing); Na2 is in 4*f* Wyckoff position, face-sharing with two Mn atoms (purple); Na3 is in 2*a* Wyckoff position, face-sharing with one Mn and one Ni/Li atom (green). d) Sodium content for all samples with the space group $P6_3/mmc$ and $P6_322$. The target Na content for each composition is shown by a dashed line. e) Unit cell parameters *a* and *c* and unit cell volume for all samples with the space group $P6_3/mmc$. The error bars are smaller than the data points, so are not visible; they are present in the respective refinements in Table 1 and Tables S2–S5 (Supporting Information). The *a* and *c* parameters of $P6_322$ are very close to $\sqrt{3}$-fold those of $P6_3/mmc$. For simplicity only results based on $P6_3/mmc$ are displayed.

We then continued our comparison among the samples focusing on the parameters obtained from the refinements in both space groups $P6_3/mmc$ and $P6_322$. Figure 4d,e summarizes the refined Na content and lattice parameters in the pristine materials. In Figure 4e we present the unit cell parameters from the simpler $P6_3/mmc$ model, as the $P6_322$ gives almost identical results (but multiplied by a factor of $\sqrt{3}$). The samples with higher Na content have a shorter interlayer distance (related to the *c* parameter). This is due to Na screening the O—O repulsion between neighboring TM layers. As the Li substitutes within the TM layer, *a* and *b* parameters present a decreasing trend. This in-plane shrinkage might be related to the average Shannon radius of the TM elements, as the average Shannon radius present a decreasing trend in general with increasing amount of Li, as listed in Table S11.[38] It may also be associated with a strengthened covalency of TM—O bonding, as the bond length decreases sequentially from 1.966(1), 1.958(1), 1.964(2), 1.949(1) Å in the lithiated samples.

Concerning the Na content (Figure 4d), compared to NM, Li-doped samples generally contain more Na as intended by design. The refinement of Na site occupancies suggests extra Na beyond 0.67 predominantly occupies the edge-sharing site, as expected by the fact that it is the most stable site in the structure. However, regardless of target stoichiometry ($x = 0.83$), we were not able to obtain refined Na contents above 0.75, as indicated by our refinements. Being less sodiated, the resulting compositions are

Table 2. Exemplary Rietveld Refinement results of a $P6_322$ structural model against powder XRD data of LNM-2.

$Na_{0.711(9)}Li_{0.164}Ni_{0.238}Mn_{0.599}O_2$				$P6_322$, $Z = 6$		
$a = b = 5.00573(4)$ Å				$R_{Bragg} = 5.85\%$		
$c = 11.0281(1)$ Å				$R_{wp} = 17.5\%$		
$V = 239.313(4)$ Å^3				$\chi^2 = 68.2$		
Atom	Wyck. sites	*x/a*	*y/b*	*z/c*	B_{iso}	Occ.
O	12*i*	0.347(1)	0.333(1)	0.6567(2)	0.91(5)	1.000
Li	2*c*	1/3	2/3	1/4	0.20(1)	0.492
Ni	2*c*	1/3	2/3	1/4	0.20(1)	0.508
Mn1	2*b*	0	0	1/4	0.20(1)	0.897
Ni_Mn1	2*b*	0	0	1/4	0.20(1)	0.103
Mn2	2*d*	1/3	2/3	3/4	0.20(1)	0.897
Ni_Mn2	2*d*	1/3	2/3	3/4	0.20(1)	0.103
$Na1_e$	6*g*	0.670(3)	0	0	2.1(2)	0.465(6)
$Na2_f$	2*a*	0	0	0	3.2(3)	0.27(1)
$Na3_f$	4*f*	1/3	2/3	0.013(1)	3.2(3)	0.24(2)

*The notation Mn_Ni stands for Mn in the Ni-rich site, and Ni_Mn stands for Ni in the Mn-rich sites; **Details on the site occupancies are given in Note S1 (Supporting Information).

thus located lower than the target ones in Figure 1. This proves that achieving Na content beyond 0.75/f.u. in P2 structures via solid state synthesis remains challenging. We also note that by using the $P6_322$ space group (Table 2; Tables S2–S5, Supporting Information), the face-sharing site is further split into two Wyckoff positions 2*a* and 4*f*. The two sites have similar occupancies, but the 4*f* site usually contributes the majority of Na in the face-sharing site due to the higher multiplicity, which is in agreement with findings by Fjellvåg et al.[33,39] These two sites are different because they share faces with different elements in the octahedra above/below, denoted as $Na2_f$ (*4f*) and $Na3_f$ (2*a*) in Figure 4c and in all Tables concerning the space group $P6_322$. $Na2_f$ sites share both faces with a predominantly Mn-filled octahedron, whereas $Na3_f$ sites share one face with a Ni/Li octahedron (Figure 4c). Therefore, we can also demonstrate the interaction between the honeycomb ordering and the Na^+/vacancy ordering: in NM, the $Na3_f$ site is essentially empty, which is expected as the empty/full sites give rise to the observed superstructure. In the Li-substituted samples, the disorder in the Ni site, which includes Li as well as some Mn, leads to a partial occupancy of $Na3_f$. Such occupancy of $Na3_f$ increases with the Li content. This further proves the fact that the Li-substitution contributes to "scrambling" the Na distribution in the alkali layer.

Our neutron refinement results in Figures S4 and S5 (Supporting Information) also confirm the features of Na content in the family of materials. In summary: i) lithiated Ni-Mn-based compositions have generally higher Na content than the end-members, but exceeding 0.75 Na/f.u. does not appear to be possible; ii) the edge-sharing site is preferably occupied; iii) in face-sharing sites, $Na3_f$ is less occupied than $Na2_f$. The LM appears to be an exception, possibly because it was synthesized by a different condition and with relatively considerable amount of carbonate impurity (6.7(2) wt.%).

2.3. Temperature-Resolved In Situ XRD

Due to the challenging synthesis of multi-metal compounds with high sodium content, and to the observation of Li_2MnO_3 into our products, we resorted to high-temperature in situ XRD to observe and understand the reaction sequence of all the tested compositions.[11] In **Figure 5**, we present the diffraction patterns of the first three materials, NM, LNM-2, and LNM-3. Prior to the formation of layered structures, we observe the Bragg reflections of the precursors, with the 110 of MnO_2 being the most intense one. The disappearance of such reflection coincides with the crystallization of our target materials, as the new 003/002 reflection of the layered oxides appears concomitantly. In the diffraction patterns of NM (Figure 5a), this temperature is ≈530 °C. Almost at the same time, a Bragg reflection ≈7.1 ° forms, which is characteristic of a P-type layered structure. We believe this can be indexed to the 003 reflection of an intermediate P3 phase, as also evidenced by the appearance of other reflections typical of P3, e.g. 015 at 20 °. P3 transforms into P2 slightly below 900 °C. After holding the temperature at 900 °C for 30 min, the P2 formation is complete. These observations of an initial P3-layer structure forming before the final P2 phase are consistent with previous observations from some of us and stem from the fact that those are the most thermodynamically favorable intermediates to form.[11] The formation of P2 on the other hand, having a small thermodynamic driving force from P3, and being kinetically slow, results in the requirement of long calcination time at high temperatures.[11]

The LNM samples are shown in Figure 5b,c, and Figure S6 (Supporting Information). It can be noticed that they experienced similar phase transitions with a lower crystallization temperature (410 °C) for the first layered phase P3. The P2 structure begins to crystallize at ≈800 °C for LNMs, lower than for NM. Both observations seem to indicate faster reaction kinetics for these materials, both for the intermediate P3 phase and the final P2 one.

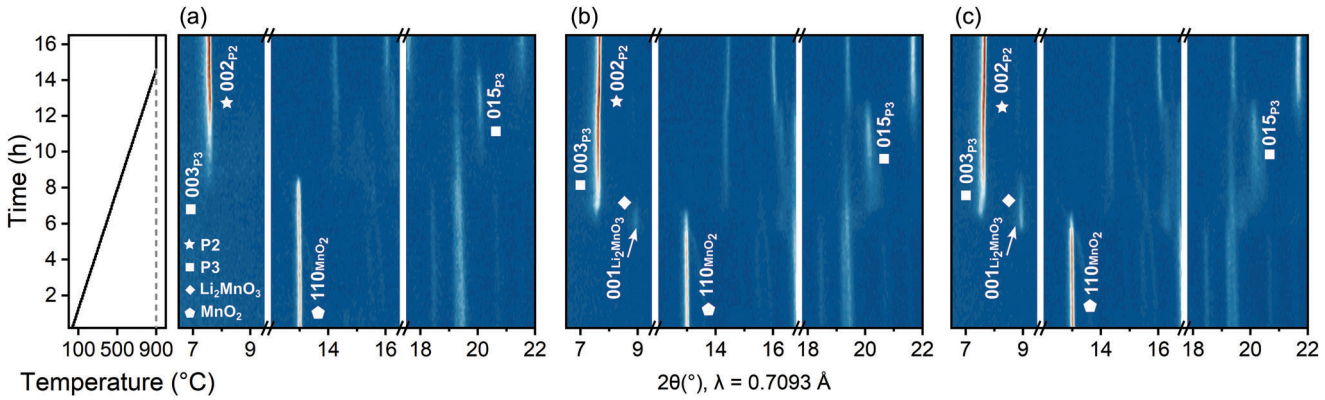

Figure 5. Temperature-resolved in situ XRD measurements during the synthesis of a) NM, b) LNM-2, c) LNM-3 at 900 °C. The starting precursors for these phases were Na_2CO_3, Li_2CO_3, NiO, and MnO_2. The reflections of P2, P3, Li_2MnO_3, and MnO_2 are marked with a star, a square, a diamond, and a pentagon respectively.

Interestingly, another intermediate phase (arrowed) starts to form at ≈370 °C, i.e., prior to the P-type layered structures, with a strong characteristic reflection near 8.4 °. Such reflection can be indexed as the 001 of the monoclinic Li_2MnO_3,[28,40] as also suggested by the fact that the reflection becomes more intense with increasing *y*. The role of Li during the synthesis reaction can then be understood: in Li-containing samples, Li reacts to form the intermediate Li_2MnO_3 phase which crystallizes as first step at a very low temperature (370 °C), most likely due to the very negative reaction energy at highly oxidizing conditions. While this does not seem to be detrimental to the crystallization of P3, it offsets the composition of the various phases. As temperature rises, Li_2MnO_3 slowly disappears indicating that Li and Mn are reintegrated into the crystal structure of P3 first and P2 later. However, as the Li content increases, Li_2MnO_3 problematically endures in the final product due to its high stability and slow decomposition kinetics, as indicated in LNM-3 in Figure 5c and LNM-4 in Figure S6 (Supporting Information).

Guided by our in situ XRD results, one can accordingly optimize the thermodynamic conditions and the choice of precursors. Due to the high Li content, the Li_2MnO_3 intermediate phase appeared to be especially detrimental for the formation of the end-member Ni-free composition LM. Given the very early formation of Li_2MnO_3, the only way to avoid it was to change precursors entirely. Hence for LM we eventually used a different strategy in terms of Mn source ($MnCO_3$ instead of MnO_2) and a lower temperature (700 °C versus 900 °C), which had also been reported to be a successful route in preparing a similar composition.[41] Another measure taken in our study was to choose 900 °C for the LNM samples to avoid further Na evaporation for higher sodiation levels in pristine powders. Our in situ XRD methodology provides a way to limit impurities forming during the reaction pathway. Moreover the results could guide optimized synthesis conditions for targeting the intermediate P3 layered structures.

2.4. 1st Cycle Electrochemical Performances

To verify the electrochemical performances of our samples, we cycled Na half cells in the voltage range of 2.0 – 4.5 V at current rate of C/10. The voltage profiles of all samples over the initial charge/discharge exhibit clearly different electrochemical behavior as a function of Li content, as gathered in **Figure 6**. The Li-free electrode NM displays three distinct plateaus. These plateaus indicate multiple biphasic processes over (de)sodiation. In particular, a very long plateau is observed for $x < 1/3$, which has been associated with the P2–O2 phase transition.[7,42] With increasing Li content, notably, all samples are able to reversibly exchange less than 2/3 of Na in the first cycle. Yet it is interesting to notice that, with the exception of NM, all Ni-containing samples deliver capacities in charge (Figure 6) in excess of the expected theoretical capacity based on the Ni-redox alone. In particular, 151.9 mAh g^{-1} versus 131 mAh g_{theo}^{-1} for LNM-2, 146.9 versus 95 mAh g_{theo}^{-1} for LNM-3, 117.6 mAh g^{-1} versus 46 mAh g_{theor}^{-1} for LNM-4. In particular, no capacity would be expected in sample LM as there is no Ni and Mn is fully or nearly fully oxidized. Since the samples were designed with fully oxidized Mn^{4+}, which was largely confirmed by the structural determination above, this indicates an important role of some O-redox activity during the first cycle. As the amount of Ni-redox available decreases with *y*, the O activity seems to instead conversely increase.

From Figure 6 one may also notice that the voltage–composition curves become visibly smoother as the Li content is increased, which may indicate that the typical phase transitions of NM have been suppressed (as we will verify in the following). From LNM-2 to LM, we also notice the development of a peculiar shape of the voltage curve, constituted by a first slopy region until roughly 4 V, followed by a flatter region beyond, which is reminiscent of the behavior observed in other P2 compounds displaying O-redox, such as those containing vacancies ($Na_{0.78}Ni_{0.23}Mn_{0.69}O_2$)[19] or Mg ($Na_{2/3}Mg_{0.28}Mn_{0.72}O_2$).[23]

In terms of reversibility, namely of the specific discharge capacity observed, we notice that for LNM-2, 3, and 4 it is reduced by ≈6%, 14%, and 35%, respectively, compared to NM. On the other hand, the Ni-free sample LM delivers the highest capacity among all members, which is surprising and most likely related to the contribution from oxygen redox and/or O_2 release, as the compounds contains no Ni.[19–22,35] Figure 6 also shows the 2nd cycle charge and discharge curves for all samples. It can be clearly observed that the large polarization of the 1st cycle is strongly decreased. As these cycles are carried out at slow rates,

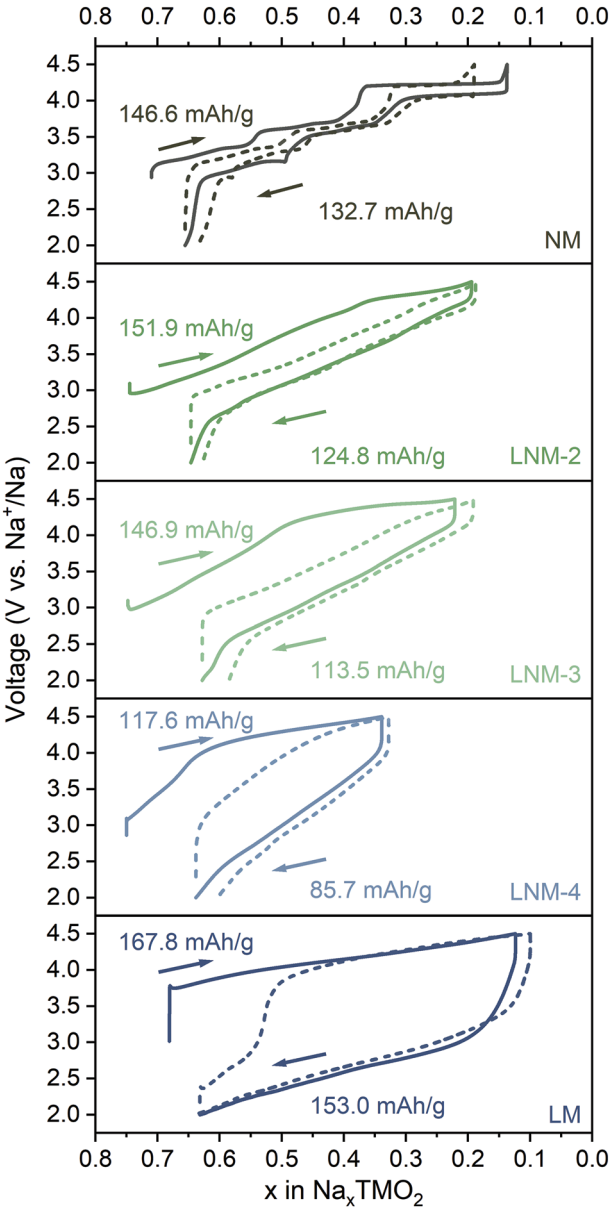

Figure 6. Galvanostatic charge/discharge curves during the first (solid line) and second (dashed line) cycle of all samples, cycled in Na half cells at C/10 current rate in the voltage window of 2.0 – 4.5 V versus Na^+/Na. Capacities in the figure refer to the first cycle.

the polarization is not due to kinetic limitations but rather to a true structural hysteresis, as we will verify in the following.

In conclusion, Li substitution appears to be capable of activating the anionic redox behavior, which allows to maintain significant specific capacities. Additionally, one should also notice the increasing polarization of the electrochemical curves during the first and second cycle. Based on this result one may then expect a certain amount of Li to be the optimal compromise between capacity, stability, and low polarization. To better understand the role of Li and to explore the structural and electronic behavior of our samples, we then employed semi-simultaneous *operando* XRD and XANES.

2.5. Semi-Simultaneous *Operando* Synchrotron XRD and XANES Investigation

Figure 7 gathers the time–voltage profile alongside XRD and XANES results for the first three members of our compounds family. Our analysis begins with an examination of the XRD data to elucidate the structural changes, followed by the analysis of the XANES data to explore the redox behavior.

When the first sample is charged (Figure 7a), the 00*l* peaks of the P2 structure shift to a lower angle. Na^+ ions are deintercalated during this process, leading to stronger interlayer O–O repulsion, and therefore increasing the *c* parameter. As the voltage reaches 3.61 V, 1/3 of the Na has been removed and a single P2 phase is maintained. The 10*l* reflections of P2 begin to disappear at 4.24 V, and a broad reflection at ≈12.3 ° gradually emerges. This new peak is characteristic of an O2 phase: 002_{O2}. Such reflection grows in intensity as the voltage reaches 4.5 V. From this point of biphasic co-existence, the lattice constants of O2 are taken into consideration by applying the space group $P6_3mc$.[41] The interlayer distance of O2 is ≈2 Å smaller than P2, while the in-plane dimensions of both hexagonal structures appear similar. This could suggest that the O2 domains are stacked along the *c* axis in P2. In any case, the vastly different *c* unit cell parameters result also in a huge volume change observed during this phase transition. If we compare the volumes of O2 and P2 ($\Delta V = V_{O2} - V_{P2}$) both at the highest charged state 4.5 V, the variation is $\Delta V/V_{P2}$ = -21.11(2)%; if the ΔV is considered to be the volume difference between O2 at 4.5 V and P2 at OCV, it becomes even greater: -22.00(1)%. This huge volume change is surely detrimental to a reversible electrochemical behavior. During discharge the reverse structural variation takes place. The phase transition process aligns with the established studies regarding P2-type $Na_{2/3}Ni_{1/3}Mn_{2/3}O_2$,[7,15,42] as we further discuss below.

Based on recent reports, we expect that the incorporation of Li within TM layers could improve the structural stability.[17,28,43] Already LNM-2 undergoes a charge process with no formation of a well-defined O2 phase, as indicated by the absence of the 002_{O2} reflection (Figure 7b). Nevertheless, one can observe a collapse of the P2 interlayer upon charging, similar to what is observed for several layered transition metal oxides when a large amount of Na (or Li, in the case of Li-ion),[41,44,45] is deintercalated. Over 3.6 V, the 00*l* and 10*l* reflections have almost vanished. Instead of entering a clear biphasic region, a mixture of P2 and an intermediate OP4 phase is formed, which is a highly defective phase, as referred to "Z"-phase according to Somerville et al.[46] Provided the resolution of the measurements and the highly defective nature of the phase, we deem that quantifying the proportion of OP4 would not be reliable, therefore only the P2 phase was modelled in the LeBail fit to obtain the lattice constants. At the beginning of charge, the interlayer distance increases similarly to the undoped sample, followed by a strong decrease. The volume shrinkage becomes most severe as the voltage is further held at 4.5 V, ultimately reaching ΔV/V = -4.77(1)%. This volume change is smaller than the -22.00(1)% difference observed between the P2 phase at OCV and the O2 phase at 4.5 V for NM, indicating a superior structural stability of LNM-2. In Figure S7 (Supporting Information) we also report the XRD patterns of the pristine samples together with the ones collected at the top of charge (4.5 V) and after the subsequent discharge to 2.0 V. As mentioned

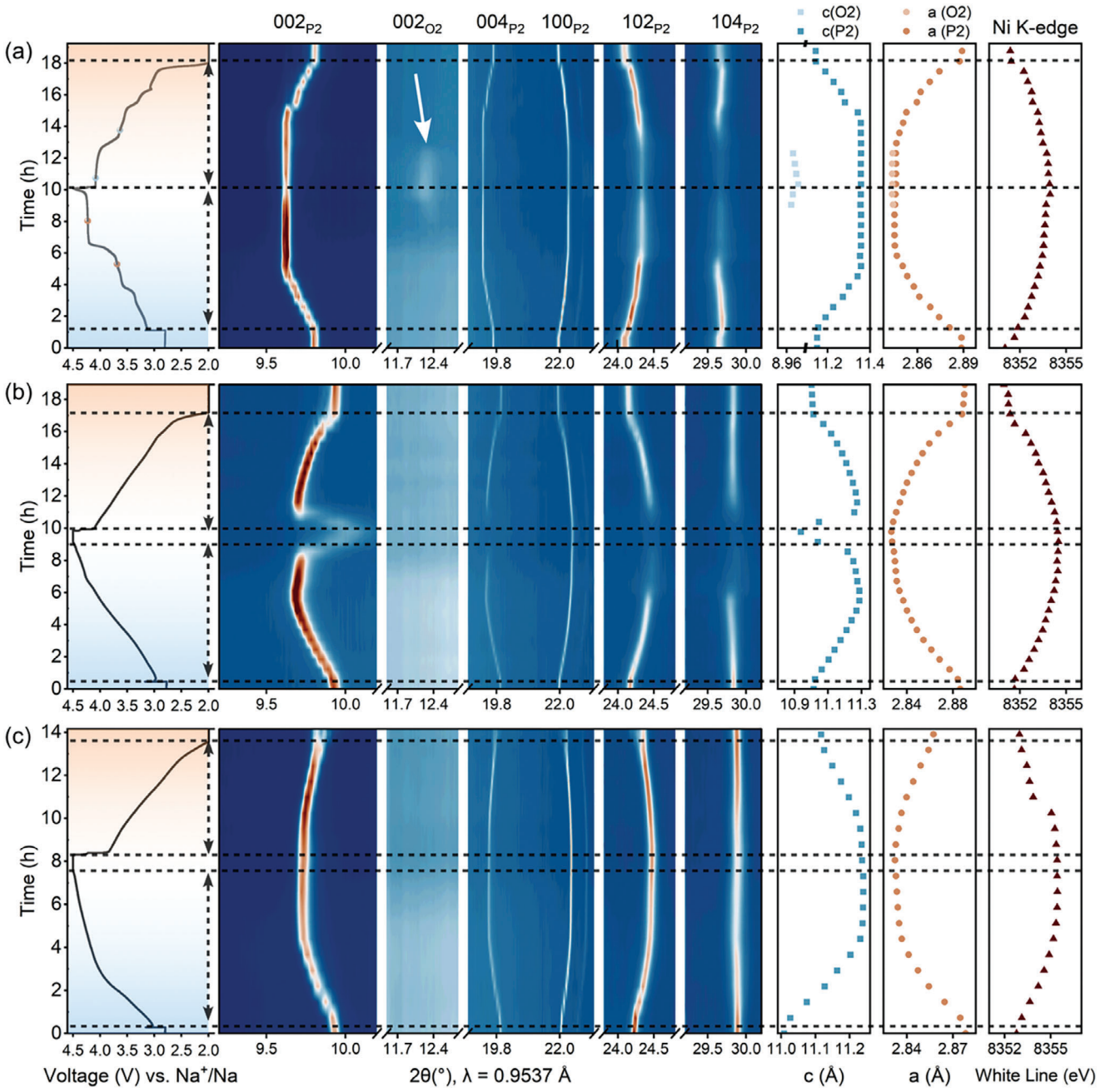

Figure 7. Structural evolution and Ni K-edge shift of a) NM ($y = 0$), b) LNM-2 ($y = 0.16$), c) LNM-3 ($y = 0.19$). From left to right for each sample, time-voltage curve (the blue region is the charge, the orange region is the discharge), 5 panels showing Bragg reflections in different angular regions (note that the color contour scale is slightly varied to improve the visibility of the peaks), unit cell parameters c and a as obtained by LeBail fit, and Ni K-edge shift obtained according to the positions of white lines (details of acquiring XANES data are described in the methods section). Notice that the three experiments are well comparable as the specific capacities obtained during charge are similar (144.2, 147.9, and 123.3 mAh g^{-1}, respectively).

above, one may clearly see in the NM and LNM-2 samples the significant broadening of the 10l reflections. For the Li-containing sample which show no sign of O2 phase, the broadening may seem to be even more pronounced. Nonetheless, upon discharge the crystallinity of the pristine P2 phase is recovered for both materials, as are the unit cell parameters: for NM, a = 2.8890(4) Å, c = 11.1504(3) Å at OCV versus a = 2.8885(3) Å, c = 11.1442(2) Å after one cycle; for LNM-2, a = 2.8865(1) Å, c = 11.0134(2) Å at OCV versus a = 2.8880(3) Å, c = 11.0126(1) Å after one cycle. From this we can conclude that both materials appear to retain their crystalline structure after one cycle, without any apparent detrimental effect of the stacking faults. However, the large volume change underwent by NM surely results in large cracks in the particles, as known from other layered materials like $LiNiO_2$ (even with volume changes of only 11–12% in that case), which ultimately results in significant material's

degradation over multiple cycles.[47] We have indeed verified the morphology of NM and LNM-2 electrodes after charging to 4.5 V in the first cycle by ex situ SEM (Figure S8, Supporting Information). The particles in the electrodes of NM display clear evidence of cracking, which was also found by Wang et al.,[42] whereas particles of LNM-2 do not, evidencing the improved morphological integrity.

In the further Li-substituted materials, this reversibility and structural stability are maintained. Figure 7c demonstrates that the interlayer collapse for LNM-3 is completely absent during the full charge and discharge cycle, with a highly stable P2 structure also at high voltage. Figure S9 (Supporting Information) shows that LNM-4 generally exhibits a similar structural stability as LNM-3, while it loses some intensity in 002_{P2} as being charged and held at 4.5 V. In Figure S10a (Supporting Information), LM is shown, with most XRD reflections undergoing no significant shift. However, the 00*l* and 10*l* reflections lose intensity during discharge (an example in the Figure S10b, Supporting Information), revealing an apparent irreversible structural degradation. The fitted lattice parameters also suggest that the structure is hardly preserved. Overall, determination of a reliable structural transition process for samples LNM-4 and LM proved to be difficult, and it is hard to determine whether they would be reproducible, which may be due to the large amount of O-redox involved, perhaps coupled with O_2 release in the cell.

Given the structural hysteresis observed from the electrochemical curves in Figure 6, one may assume a certain amount of transition metal migration may be occurring, as also suggested in the literature.[48] We use our *operando* XRD data to verify this hypothesis comparing the P2 materials at OCV and after one cycle. The Rietveld refinements in Figure S11 (Supporting Information), and the related results in Tables S12–S14 (Supporting Information), demonstrate that no significant reduction in electronic density occurs in the transition metal sites after one cycle. However, a close look at the superstructure reflection typical of honeycomb ordering ($P6_322$ space group), shown in Figure S12 (Supporting Information), reveals a clearly reduced intensity. This demonstrates that redistribution of the metals occurs during the first cycle, even though any migration appears to be reversible as the total amount of transition metals does not decrease.

The evolution of the Ni K-edge is analyzed based on the shift in the white line position, as reported in Figure 7. In Figure S13 (Supporting Information) the shift can also be appreciated on the 1st derivative plot of the XANES spectra. The absorption edges shift to higher energies during charging, and return to the original position during discharge, indicating a reversible Ni-redox activity. Generally, the energy difference between the OCV and the highest charge state at 4.5 V is ≈2.9, 2.8, 2.6, and 2.4 eV for NM, LNM-2, LNM-3, and LNM-4, respectively. An energy jump of ≈2 eV is considered to correspond with the shift of one valence state for Ni.[17,49] This energy difference is also consistent with what we measured from $LiNiO_2$ (Ni^{3+}, 8352.6 eV) and NiO (Ni^{2+}, 8350.3 eV). It is possible that either Ni ions are not fully oxidized to 4+ at 4.5 V, or in the pristine state the oxidation state is already above 2+. The detailed XAS measurements at different states of charge are presented in **Figure 8** and Figures S14–S17 (Supporting Information). By comparing the XAS spectra of the pristine materials with NiO and $LiNiO_2$ reference spectra in these figures,

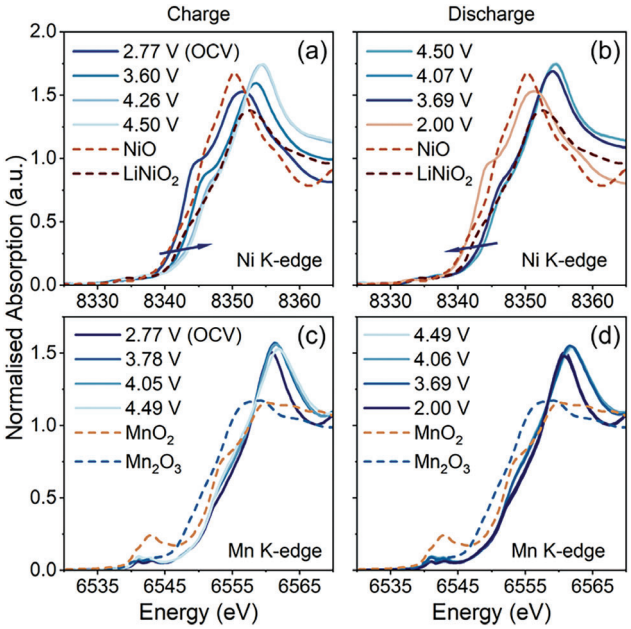

Figure 8. XANES spectra of LNM-2, plotted as a function of the different voltages applied (*operando*). a) Ni K-edge during charge, b) Ni K-edge during discharge, c) Mn K-edge during charge, d) Mn K-edge during discharge.

we find it more likely that Ni ions in the pristine compounds are not perfectly divalent, but rather a mixture of 2+ and higher oxidation states. As we also observe in Figure S14 (Supporting Information), from the LNM-2 on the average oxidation states of Ni are actually higher than that in $LiNiO_2$. This makes sense as the actual sodium content in the samples is lower than the nominal one (for example, in LNM-2 it is found to be 0.75 versus 0.83 nominal, hence the expected average Ni oxidation state is +2.84). Mn ions are instead tetravalent as they match the position of the MnO_2 reference sample and appear to remain inactive during the whole cycle (Figure 8; Figures S14–S17, Supporting Information). It is noted that in the lithiated samples, the Mn pre-edge shows a slight increase at the top of charge, while that of NM barely present any change. An explanation to such behavior is proposed in the next section based on the ab initio calculations.

Here we evaluate in more detail the evolution of the Ni K-edge upon charging for the four samples where Ni is present, as shown in **Figure 9a**. Based on the shape of the electrochemical curves and on the evolution of cell parameters, we would expect a non-monotonic evolution of the Ni K-edge position upon charging. In fact, we notice that the Ni edge shifts at the beginning to higher energies for all samples; however, while the trend continues almost linearly for NM throughout the whole charge, the increasing amount of Li appears to result in a plateau where the Ni K-edge does not shift anymore, at which point the oxidation of Ni is almost complete and further charge must result from other forms of charge compensation. We select the point at which the Ni-redox appears to stagnate based on the white line change: $\Delta E = E_{i+1} - E_i$, $2 \leq i < i_{max}$, where i represents the different data points of the experiment, each with decreasing Na concentration x. The white line change versus x in Na_xTMO_2 of all four samples is presented in Figure S18 (Supporting Information). This curve

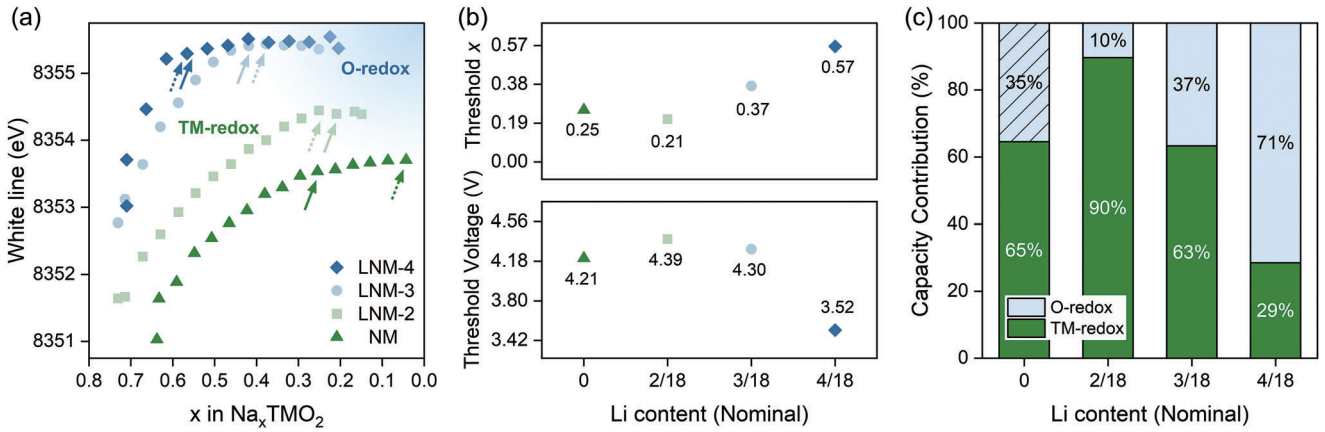

Figure 9. a) Ni K-edge evolution upon charging. The full arrows point out the beginning of O-redox based on the white line energy change; the dashed arrows specify the beginning of O-redox based on nominal Ni content in the refined compositions. b) Threshold voltage and x of O-redox onset. c) Contribution to the observed capacity by TM-redox and O-redox, respectively. For NM which represents an exception in the evolution of the curve, a shaded area is visualized indicating O-redox is present also based on results from the literature.[50,51]

approximates the derivative of the edge position. If one assumes a linear shift of the edge position followed by a constant region, the white line change should look like a step function, constant initially and zero after a certain point. Indeed, this is exactly how LNM-4 sample looks, with a step occurring near composition $x = 0.6$. For the other samples the behavior is less ideal, yet we can always clearly distinguish a decrease of the white line change. To distinguish the capacity contributed by different redox couples for each sample, we assume here a threshold of 0 ± 0.1 eV for the white line change (gray dashed lines in Figure S18, Supporting Information). When at least two consecutive points lie within this band, the white line change is considered to have reached a stable region with insignificant oscillation, indicating Ni-redox is therefore marginally contributing. These points are specified with the solid arrows in Figure 9a. In comparison, we also marked with dashed arrows the limiting "theoretical" x values beyond which Ni should run out of redox ability, based on the full nominal Ni content for each sample. The NM reaches this point when fully charged, evidencing that it could potentially have TM-based capacity only, however our data show a clear discrepancy from this ideal behavior as the full arrow indicates that already beyond $x = 0.3$ the Ni-redox is not the dominant charge compensation mechanism anymore. Interestingly, we observe for all other samples a clear capacity beyond Ni-redox at high state of charge, which matches closely the "theoretical" amount as proved in Figure 9a (notice the vicinity of dashed and full arrows for LNM-2, LNM-3, and LNM-4). A final consideration can be made from Figure 9: the materials are not all reaching the same edge energy position while charged to 4.5 V. It is hypothesized that, even though all samples are nominally close to 4+ at the end of charge, the local environment of Ni ions in the four samples is different. In NM, Ni ions in TM layer are surrounded only by Mn. With Li substitution, Ni is diluted and has significant amounts of Li around, which greatly alters the local electronic structure. A similar behavior has been observed in other studies on related materials.[22]

While all samples continue to deliver capacity when charged to high voltage, we determined that they reach a threshold voltage V_T and threshold Na content x_T where the anionic redox takes place and starts to dominate. Based on the transitioning points found with the above-mentioned criteria, such thresholds are shown in Figure 9b, as well as the respective capacity contribution by TM-redox and O-redox in Figure 9c. Interestingly, we observe that the threshold voltage remains very high for NM and LNM-2 and LNM-3, dropping only for LNM-4. Hence the former materials only display O activity beyond 4.3 V, while the latter already at very low voltage (3.52 V).

On the other hand, the Na content threshold shifts linearly for all lithiated materials, going from $x = 0.21$ in LNM-2 to $x = 0.57$ in LNM-4. This indicates that the activation of O-redox is more closely related to the Ni and Na content, rather than the applied voltage. However, care must be taken. While these Li-containing materials display a clear bimodal behavior in the Ni K-edge shift (Figure 9a, a strong shift followed by a flat region), it may be noticed that the shift never ends for NM until the end of charge. Instead, the slope of the curve decreases at high states of charge (Figure 9a, dark green curve), likely indicating more hybridized/overlapping Ni—O states as also expected by the overlapping partial density of states (pDOS) of O and Ni reported by Zuo et al.,[50] which we also confirm with our own calculations for pristine NM (see **Figure 10a** discussed below, hybridized band of Ni—O below the Fermi level). A threshold voltage of 4.21 V is also determined from its white line change in Figure S18a (Supporting Information), with corresponding threshold $x_T = 0.25$. In agreement with the literature on the NM material, it is possible to state that O-redox is indeed activated in this material already from 4 V, i.e., from the beginning of the P2–O2 phase transition at $x = 0.33$, also resulting in O_2 release later on.[48,50,51] While in NM the O and Ni pDOS significantly overlap at low Na contents, the clear bimodal behavior of the Li-containing samples seem to indicate a sharper separation of the O orbitals at higher voltages from the Ni ones at lower voltages. In this respect, the Li-containing material LNM-2 reported here may represent then the compound with the lowest anionic redox contribution among the family.

Other than the *operando* XRD/XANES data, which give us access to average electronic and structural information on the samples at the top of charge and after 1 cycle, we have measured also ex situ EXAFS for the undoped NM and the lithiated sample

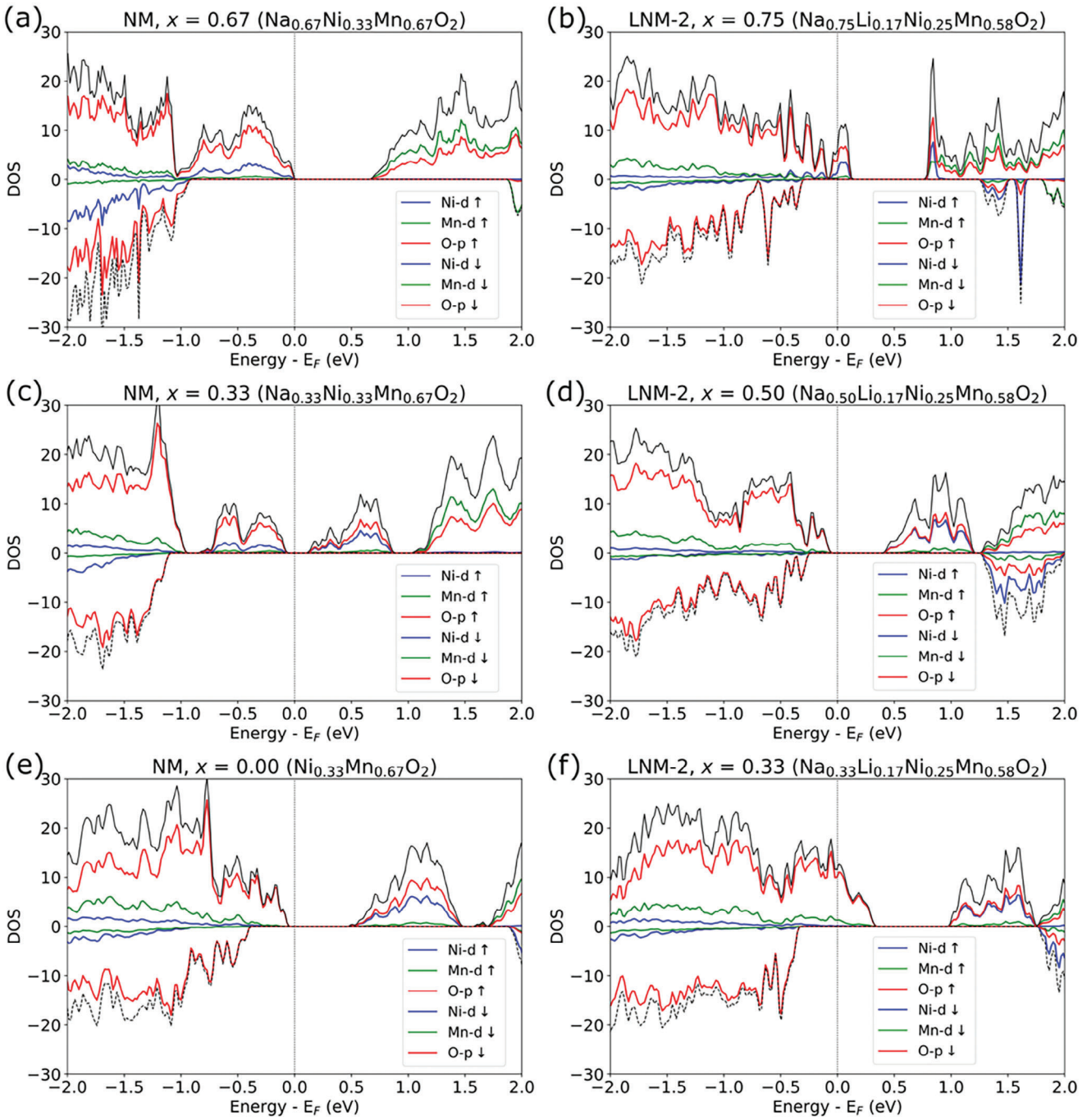

Figure 10. a) pDOS of pristine NM with $x = 2/3$ for Na_xTMO_2 (nominally Ni^{2+}). b) pDOS of the pristine LNM-2 model with $x = 3/4$ (nominally Ni^{3+}). c) pDOS of partially charged NM with $x = 1/3$ (nominally Ni^{3+}. d) pDOS of the partially charged LNM-2 model with $x = 1/2$ (nominally Ni^{4+}). e) pDOS of charged NM with $x = 0$ (nominally Ni^{4+}). f) pDOS of the partially charged LNM-2 model (nominally $Ni^{4.67+}$ or $Ni^{4+}O_2^{-1.91}$). Note that the composition "LNM-2" calculated here, because of the supercell constraints, has rather a composition intermediate between the LNM-2 and LNM-3 samples.

LNM-2, to verify by a bulk probe if locally around the Ni and Mn cations any sign of irreversible degradation following the O-redox upon charge could be detected. The fittings of ex situ EXAFS are included in the Figures S19 and S20 (Supporting Information). The fitted parameters are included in the Tables S15 and S16 (Supporting Information). During charge the Ni—O bond lengths, as well as the in-plane Ni-Mn interatomic distance, are drastically changed in NM. On the other hand, these distances are almost constant in LNM-2, indicating much reduced structural variations. These results show that Li-containing samples display less significant structural change upon charge, proving that lithium's presence can mitigate structural instability even when probed locally in the first and second coordination shell around Ni.

2.6. Ab-Initio Calculations

The above findings are further investigated by DFT calculations, using an approximate model for NM and LNM-2 based on the measured compositions. Due to modeling limitations, the model for LNM-2 has a sum formula that lies in between the experimental sum formulae of LNM-2 and LNM-3. The pDOS calculated for NM and LNM-2 are reported in Figure 10. In pristine NM (Figure 10a), as in pristine LNM-2 (Figure 10b), hybridized Ni—O states exist at the Fermi level, but in the latter they are only partially occupied due to the higher oxidation state of Ni, nominally already +3 in the model. At $x = 0.5$ in LNM-2, the nickel ions in the model reach a nominal oxidation state of +4 and the upper hybridized Ni—O states (Figure 10d) are fully unoccupied, as it happens for charged NM with $x = 0.0$ (Figure 10e). Before being fully desodiated, NM goes through composition $x = 0.33$ (Figure 10c), where it can be noticed that the band below the Fermi energy responsible for the last part of the charge is of hybridized Ni—O antibonding character. After full charge in NM and at $x = 0.5$ in LNM-2, a significant spin remains at the nickel ions (≈0.4 for LNM-2 and 0.66 for NM), indicating that they are not fully oxidized to their nominal oxidation state, for which a low-spin d^6-configuration with a magnetic moment of 0 is expected. Accordingly, this suggests that the Ni—O electronic levels are contributing to the redox reaction at that point, as mentioned above and already pointed out for NM at $x = 0.33$ by Zuo et al.[50] From $x = 0.5$ to $x = 0.33$ for LNM-2 (Figure 10f), the spin of Ni remains the same, indicating no further oxidation toward an oxidation state of +4. This is quantitatively at variance to the observed K-edge behavior of Ni, likely due to the general limitations of PBE+U and the choice of the system, which is in between LNM-2 and LNM-3. At $x = 0.33$, the main contribution to the bands at the Fermi level originates from the oxygen atoms neighboring the Li ions (Figure S21, Supporting Information). This suggests that pure oxygen redox becomes the dominant mechanism for charge compensation during charging for $x < 0.5$. These findings explain the flattening seen for the Ni K-edge of LNM-2 in Figure 9a and the different behavior of LNM-2 and NM, as the oxygen redox occurs in two different kinds of bands. In LNM-2, the oxidation affects only initially the hybridized Ni—O bands, before it gradually transitions into oxygen redox in pure, non-bonding oxygen bands. As a final remark to Figure 10f, we notice the pDOS at $x = 0.33$ is mostly dominated by O states, but a slight Mn contribution is present. While this is very small and Mn does not appear to participate to the charge compensation according to the XANES results, this contribution of Mn to the pDOS near the Fermi level may explain the variation of the Mn pre-edge observed in our XANES results at high state of charge in the Li-containing samples (Figure 8, and Figures S14–S17, Supporting Information).

The existence of metastable partly oxidized oxide anions, possibly as dimerized O—O in the lattice eventually turning into molecular O_2, is often found to be responsible for the contribution of anionic redox.[19,35,52,53] Further determination of the state of oxygen can be realized by combining O_2 gas analysis and other local techniques including RIXS for oxygen and EXAFS for TM,[22,54] which is however beyond the scope of our study. The increased difficulty in obtaining reliable electrochemical results for multiple cycles for samples LNM-4 and LNM-5, also in the *operando* experiments, indicates that probably not only reversible O-redox is responsible for the charge compensation, but also O_2 release is present, followed by irreversible structural transformations. In fact, in a parallel study, we investigated the gas evolution behavior of all samples. We find O_2 and CO_2 release during the 1st cycle in all compositions examined in this work, in increasing amount with increasing Li content.[52] This further demonstrates the interplay between O-redox, O_2 release, and transition metal reversible migration, leading ultimately to the hysteresis present in Figure 6.

2.7. Long-Term and Rate Performances

The long-term cycling performance of all the samples is shown in **Figure 11**. The cycling program consists of the following steps in sequence: 5 cycles at C/10, 50 cycles at C/2, one cycle at C/10, another 50 cycles at C/2, and one final cycle at C/10. After the complete cycling test, the undoped member NM shows a significant capacity decay. By comparing the slow cycles 5 and 107 at C/10, one can observe only ≈57% capacity retention. The doped samples provide instead better performance: in the last slow cycle, LNM-2 delivers a discharge capacity of 108.7 mAh g^{-1}, which corresponds to an improved capacity retention of ≈92% (versus 118.2 mAh g^{-1} after cycle 5 also at C/10). LNM-3 offers slightly lower capacity than LNM-2 overall. Despite that, it delivers 110.8 mAh g^{-1} after cycle 5 at C/10, and 106.9 mAh g^{-1} after all 107 cycles, i.e., a capacity retention of ≈96%. LNM-4 appears to have even better retention capability, whereas it delivers the least capacity due to its hugely reduced Ni content, which limits any further usage. Interestingly, despite our previous observations, the Ni-free composition could deliver a noticeably higher capacity than the others in the whole material's family and maintain such capacity for more than 100 cycles. Reported by Yabuuchi et al. in a work specifically on a very close composition P2-$Na_{5/6}[Li_{1/4}Mn_{3/4}]O_2$, the decent stability of such material could be a consequence of the in-plane cation rearrangements, including partial lithium extraction and partial oxygen loss from TM layers, which activates the originally inactive Mn^{4+}.[41] This intriguing behavior, as well as whether these observations hold in full cells, will be the object of further investigation.

While the Li incorporation helps enhance the cycling stability and structural reversibility, the trade-off is a marked loss in the capacity due to the less Ni-redox. In quest of practical applications compromising both cycling stability and capacity, we suggest Li amount comprised between 0.16 (as in LNM-2) and 0.19 (as in LNM-3), as these two compositions deliver the most promising performances overall. This is likely related to the appropriate Li content, able to reduce volume change at high voltage but maintaining a sufficiently large specific capacity (>100 mAh g^{-1}) and a moderate amount of O-redox and hence moderate ensuing polarization.

To further strengthen the promising performances of LNM-2 we measured rate capability tests as reported in Figure 11b. Here it can clearly be seen that LNM-2 performs better than both NM and LNM-3. After an initial capacity of ≈120 mAh g^{-1} at C/10, ≈90 mAh g^{-1} are retained at C rate (set at 1C = 200 mA g^{-1}) and ≈30 mAh g^{-1} at 10C rate. For comparison, NM only retains ≈50 mAh g^{-1} at 1C rate and no capacity at 10C, while LNM-3 retains ≈70 mAh g^{-1} at 1C and 10 mAh g^{-1} at 10C. We argue that

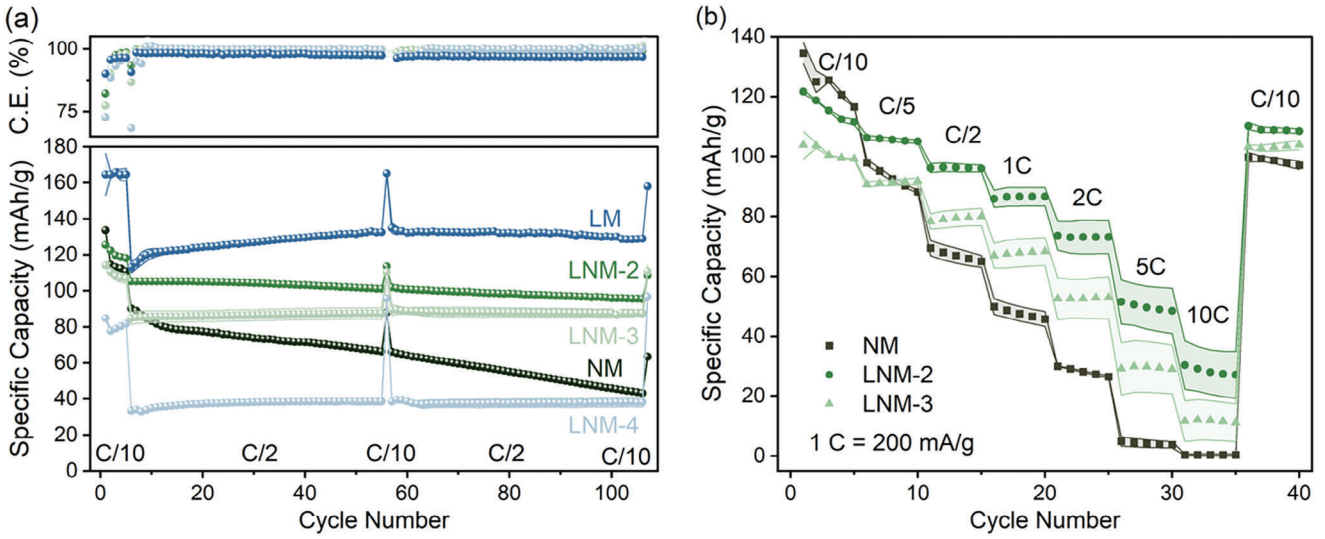

Figure 11. a) Cycling stability of the series of P2 materials in Na coin half cells. The columbic efficiencies of the 56th cycle and the 107th cycle are not present as a rate of C/10 was applied among 100 cycles of C/2. b) Rate capability of NM, LNM-2, and LNM-3. The error bands represent 2 or 3 coin cells.

LNM-2 having faster Na kinetics than NM is due to the avoided phase transitions and the more disordered Na positions, while not having an exceedingly high amount of O-redox as in LNM-3. Finally, we test LNM-2 in full cell configuration versus a hard carbon anode (Figure S22, Supporting Information). Here one can already observe better capacity retention in the doped material LNM-2 after 100 cycles, with respect to the undoped NM. In addition, the cycling profiles of the initial two cycles for the full cell shows comparable charge and discharge capacities as delivered in half cells. Further studies will be focused on improving full cell configurations.[52]

3. Conclusion

In this work we investigated the impact of Li substitution in a series of P2-type layered oxides, with nominal compositions of $Na_{5/6}Li_yNi_{5/12-3y/2}Mn_{7/12+y/2}O_2$ (y = 2/18, 3/18, 4/18, 5/18; and $Na_{2/3}Ni_{1/3}Mn_{2/3}O_2$) as positive electrode materials for Na-ion batteries. To push the sodium content in these P2 structures for better sodium storage performance via solid-state synthesis, we tuned the stoichiometry in the precursors. We obtained compositions with up to 0.75 Na per unit formula, while further sodiation remains a challenge.

We provided a careful structural study of our samples by using x-rays and neutrons and demonstrated that all samples present some amount of honeycomb ordering, which can be better described in a $P6_322$ space group. The ordering is visible either via neutron (Ni/Mn) or via x-ray diffraction (Li/Mn). On the other hand, only $Na_{2/3}Ni_{1/3}Mn_{2/3}O_2$ presents an additional Na^+/vacancy ordering, which is eliminated by the presence of Li, which increasingly forces Na to redistribute over the Na_e and the two Na_f sites. Furthermore, the extra Na beyond $Na_{0.67}$ is found to mainly occupy the edge-sharing sites in the hexagonal structures, which is more stable. Via in situ temperature-resolved XRD we observed the phase evolution processes during synthesis, in order to optimize and understand the process. The formation of an intermediate Li_2MnO_3 structure is observed early during the heating process. Although it is not found to inhibit the crystallization of further P-type layered structures, it remains as byproduct especially in the highly lithiated compounds.

Electrochemically, this family of P2 materials show an increasing trend of polarized hysteresis in the first and, to a lesser extent, second charge and discharge cycle, which evidences the likely contribution of O-redox and transition metal migration. By exploiting semi-simultaneous *operando* XANES and XRD to understand the structural evolution and redox behavior during this process, we verified that Li in the TM site eliminates phase transitions at high voltage. In the lithiated samples, an increasing Li amount also relates to the presence of the O-redox starting at lower states of charge. However, our detailed XANES and DFT combined analysis demonstrates that the NM samples have a peculiar behavior already displaying significant O-redox contribution around x = 0.33, despite the "theoretical" availability of further Ni redox. On the other hand, LNM-2 shows a far lower amount of O-redox contribution as compared to NM, which we attribute to the different density of states around the O ions. In fact, the anionic redox in NM is rooted in Ni–O hybridized energy states, while in LNM-2 it is rooted in pure O non-bonding states. The transition metal migration is proven to occur in parallel during the first cycle, yet it is reversible and it only results in a lower degree of honeycomb ordering.

Ultimately, LNM-2 appears to be the material with the broadest range of Ni-based charge compensation, which may be responsible for its optimal electrochemical performances. In fact, among the five P2 materials synthesized, LNM-2 with 0.16 Li/f.u. delivers the best balance of cycling stability, capacity and rate capability. This composition ($Na_{0.745(6)}Li_{0.164(4)}Ni_{0.238(1)}Mn_{0.599(3)}O_2$) can be considered as a new starting point for the development of Li-substituted P2 sodium layered oxides. Studies extending our findings to full cells and towards a better understanding of the oxygen release in the compounds are under way to confirm the promise of this class of materials.

4. Experimental Section

Materials Synthesis: Stoichiometric precursors were introduced in zirconia jars and mixed by a SPEX-8000M ball-mill for 1 h. The sodium and lithium precursors were Na_2CO_3 (Alfa Aesar, 99.95%) and Li_2CO_3 (Alfa Aesar, 99.998%), respectively. The nickel precursor was NiO obtained from decomposition of $Ni(OH)_2$ (Alfa Aesar, 99.999%) after heating at 400 °C for 6 h. The manganese precursor was MnO_2 (Thermo Scientific, 99.9%) for NM, LNM-2, LNM-3, LNM-4, and $MnCO_3$ (Sigma-Aldrich, 99.9%) for LM.

The mixed precursors were pressed into pellets and then calcined in air. NM was calcined at 950 °C for 12 h; LNM-2 was calcined at 900 °C for 12 h, followed by intermediate grinding and subsequent re-heating at 900 °C for 8 h; LNM-3 and LNM-L4 were calcined at 900 °C for 12 h in a single step. The heating and cooling rate was 5 °C min^{-1} for these calcinations. LM was calcined at 550 °C for 1 h, followed by 700 °C for 12 h, with a heating rate of 5 °C min^{-1} and a cooling rate of 5 °C min^{-1}, and then washed with distilled water to remove the impurity of Na_2CO_3. All synthesized products were transferred to an argon-filled glovebox (200 B, MBraun, Germany; $H_2O < 0.1$ ppm, $O_2 < 0.1$ ppm).

Materials Characterization: Powder x-ray diffraction (XRD) patterns were measured by a Stoe StadiP diffractometer (acquisition on sample powders packed in a borosilicate glass capillary of 0.5 mm diameter, in the 2θ range of 2–75 with a step size of 0.015°). The diffractometer was equipped with monochromatic Mo-Kα_1 ($\lambda = 0.709319$ Å) radiation and with a MYTHEN 1K detector. Rietveld refinements were performed with the FullProf Suite.[55,56]

In situ temperature-resolved XRD measurements were performed in the same diffractometer by using a Stoe ST2K furnace. Samples were first prepared in the form of powders, which were filled in a sapphire capillary of 1 mm diameter, which was then inserted in the furnace and heated under ambient air. Patterns were recorded in the 2θ range of 2–37° with a step size of 0.015° for 10 min at each temperature. The furnace had a rocking motion to improve powder averaging.

Neutron diffraction (ND) was carried out on the D2B neutron diffractometer at the Institut Laue-Langevin (ILL). Powder samples were put into cylindrical vanadium cans and measured in transmission geometry at $\lambda = 1.59485(3)$ Å (where the λ value was refined using FullProf software). LM sample measured by ND was not washed, thus containing Na_2CO_3 and was refined with this phase considered.

Scanning electron microscopy (SEM) images and energy dispersive x-ray analysis (EDX) were performed using a ThermoFischer Scientific Phenom ProX microscope. The images were captured at an acceleration voltage of 10 kV on the sample particles, with a magnification of 10000 times, using a secondary electron detector (SED).

Electrochemical Characterization: The electrodes of cathode were prepared by tape casting. 85 wt.% of active cathode materials, 7.5 wt.% of conductive carbon (Super P, Alfa Aesar, 99%), and 7.5 wt.% of PVDF (polyvinylidene fluoride) were mixed in a centrifugal mixer (THINKY ARE-250). PVDF had been previously prepared as a solution in NMP (*N*-Methyl-2-pyrrolidone, Sigma-Aldrich, 99.5%). The resultant slurry was casted on the aluminum current collector. The loadings of the electrodes for NM, LNM-2, and LNM-3 reached 5–7 mg cm^{-2}, whereas for LNM-4 and LM were ≈3–4 mg cm^{-2}. The loadings of the two most lithiated compositions were kept low to avoid jellification while casting.

The 2032 coin half-cells were assembled in an argon-filled glove box (200 B, MBraun, Germany; $H_2O < 0.1$ ppm, $O_2 < 0.1$ ppm) with metallic sodium (prepared from dry stick, thermo scientific) as a counter and reference electrode, porous glass fiber separators (Whatman, GF/A grade) and 80 µL of electrolyte. The electrolyte was 1 M sodium hexafluorophosphate ($NaPF_6$) in ethylene carbonate/dimethyl carbonate (EC:DMC = 1:1 wt.%) with 2 wt.% additive of fluoroethylene carbonate (FEC). The galvanostatic charge–discharge measurements were performed on a temperature-controlled battery system (Arbin Instruments, USA; 25 °C). The half cells were cycled between 2.0 and 4.5 V versus Na^+/Na^0 at specific current rates where 1C = 200 mA g^{-1}.

The full cells were assembled in the same way using hard carbon as the anode. The electrolyte and assembly conditions remained unchanged as half cells. The hard carbon was synthesized in house from cellulose (Sigma-Aldrich, microcrystalline, powder, 20 µm) through a 2-step heat treatment: 300 °C in synthetic air for 12 h, followed by 1400 °C in Ar atmosphere for 1 h. The anode electrodes were prepared by tape casting. 95 wt.% of active anode materials, 5 wt.% of binder (CMC:SBR = 50:50 wt.%; CMC: carboxymethylcellulose, Dupont; SBR: styrene-butadiene rubber, MTI Corp.) were mixed in a centrifugal mixer (THINKY ARE-250). The binder of CMC:SBR had been previously prepared as a 7.5 wt.% solution in water (VWR chemicals). The slurry was casted on the aluminum current collector. The loadings of the electrodes were 2–3 mg cm^{-2}. The full cells were cycled between 1.0 and 4.5 V at the specific current rate of 1C = 200 mA g^{-1}. The areal N/P ratio was balanced to 1.1. The cycling protocol consists of the following steps in sequence: 5 formation cycles at C/20, 50 cycles at C/3, one cycle at C/20, another 50 cycles at C/3, and one final cycle at C/20. CCCV was applied for all charging steps, with a cutoff current corresponding to rate of C/30. The specific capacity was reported based on cathode mass.

Operando Structural and Electrochemical Characterization: Semi-simultaneous *operando* x-ray absorption spectroscopy (XAS) and x-ray diffraction (XRD) analysis were carried out in transmission mode at NOTOS beamline at ALBA Synchrotron Light Source, Barcelona, Spain. The synchrotron light coming from a bending magnet had been first vertically collimated, then monochromatized using two pairs of liquid-cooled Si(111) crystals and finally focused on the sample position down to ≈800 × 500 μm^2. Si and Rh stripe coatings of the two mirrors were opportunely chosen to guarantee the higher harmonics rejection. Energy calibration was done by measuring the XANES spectra of an Mn o Ni foils.

The tested cells were assembled the same way as the regular lab procedure mentioned above, except for the usage of different cell cases and spacers. The cell cases and spacers for the *operando* usage had an open circular hole in the center to allow better x-ray transmission. Kapton windows were glued and covered the holes on both sides of the cell cases. A total of 4 cells were mounted in parallel on a customized coin cell holder, which was controlled by a BioLogic Potentiostat testing system. By translating the beam position, it was possible to scan the 4 cells in sequence. It should also be noted that due to the limitation of the coin cell holder, e.g., lacking a rocking motion, the powder averaging was more limited in this case.

XRD patterns were acquired at 13 keV (0.9537 Å) in the 2θ range of 7–50° for 15 s using the Mythen detector. Data collection for XANES was conducted in transmission mode at the Ni K-edge and the Mn K-edge with a simultaneous reference spectrum of metallic Ni and Mn foil, respectively. Acquisition time for a XANES spectrum was ≈4 min each: The scan range for Ni was 8240–8740 eV, with a 0.33 eV step resolution, and a dwell time of 0.12 s; For Mn, the scan range was 6470–6970 eV, with a 0.33 eV step resolution, and 0.10 s per step. The data were treated with the ATHENA package.[57] 8333 eV for Ni and 6539 eV for Mn were used as an absorption edge energy position. As a result, the overall collection time for each sequence was ≈40 min for 4 cells, including the measurements of XRD, Ni K-edge XANES, Mn K-edge XANES, and configuration changes. On average, ≈10 min was required for each cell over each sequence. As it took only a very short time to switch between different measurements, the coupled usage of these two characterization techniques was described as "semi-simultaneous".

Ab-Initio Calculations: The density functional theory calculations were carried out in the plane-wave program package VASP[58–60] with PAW pseudopotentials,[61] the generalized gradient approximation functional PBE,[62] and the Grimme D3(BJ) dispersion correction with Becke-Johnson damping.[63,64] For all calculations, a cutoff energy of 520 eV was chosen in accordance with the most effective cutoff used in the Materials project.[65]

The structure models for LNM-2 and NM[7–9] were based on the general unit cell of the P2 structure type. The program supercell[66] was used to generate all possible configurations of a 3 × 2 × 1 supercell with the approximate atomic composition of LNM-2 and NM. In the case of pristine LNM-2 (75% Na sites occupied), the corresponding model contains 9 Na, 2 Li, 7 Mn, 3 Ni, and 24 O, and in the case of pristine NM (66.7% Na sites occupied), it contains 8 Na, 8 Mn, 4 Ni, and 24 O. From all generated

configurations, the configuration with the lowest Coulomb energy was selected for the subsequent structure optimization and calculation of the projected density of states (pDOS). The desodiated structures for LNM-2 at 50% and 33.3% occupied Na sites were obtained by a stepwise removal of sodium ions in a way that minimizes the Coulomb energy at every step, which was calculated using the Ewald summation tool in pymatgen.[67] For the optimizations, a force convergence criterion of 0.01 eV $Å^{-1}$ and an energy convergence criterion of 1×10^{-5} eV were used as well as a k-point grid density of $3 \times 4 \times 2$ for the structure supercells. All optimized structures can be found in the Supporting Information. For the calculation of the pDOS, the energy convergence was tightened to 1×10^{-7} eV and the k-point grid density was increased to $6 \times 9 \times 4$. The pDOS itself was plotted with the python package pyprocar.[68]

Supporting Information

Supporting Information is available from the Wiley Online Library or from the author.

Acknowledgements

The authors acknowledge ALBA for the allocation of synchrotron XRD, XANES, and EXAFS measurements at the beamline NOTOS (Proposal IDs: 2022097072-mbianchini, 2023097902-mxu). The use of the neutron diffractometer D2B and the support of Emmanuelle Suard is gratefully acknowledged (Beamtime 5-23-775). This work was partly funded by the European Union (ERC StG 4SBATT, project 101 039 399). Views and opinions expressed are however those of the author(s) only and do not necessarily reflect those of the European Union or the European Research Council Executive Agency. Neither the European Union nor the granting authority can be held responsible for them. The computations in this work are supported by the Deutsche Forschungsgemeinschaft (DFG, German Research Foundation) – INST [91/242–1] FUGG.

Open access funding enabled and organized by Projekt DEAL.

Conflict of Interest

The authors declare no conflict of interest.

Data Availability Statement

The data that support the findings of this study are available from the corresponding author upon reasonable request.

Keywords

battery, cathode, in situ, Na-ion batteries, XRD/XANES

Received: December 24, 2024
Revised: January 22, 2025
Published online:

[1] H. S. Hirsh, Y. Li, D. H. S. Tan, M. Zhang, E. Zhao, Y. S. Meng, *Adv. Energy Mater.* **2020**, *10*, 2001274.
[2] R. Usiskin, Y. Lu, J. Popovic, M. Law, P. Balaya, Y.-S. Hu, J. Maier, *Nat. Rev. Mater.* **2021**, *6*, 1020.
[3] S. P. Ong, V. L. Chevrier, G. Hautier, A. Jain, C. Moore, S. Kim, X. Ma, G. Ceder, *Energy Environ. Sci.* **2011**, *4*, 3680.
[4] C. Delmas, C. Fouassier, P. Hagenmuller, *Phys. B+C* **1980**, *99*, 81.
[5] R. Berthelot, D. Carlier, C. Delmas, *Nat. Mater.* **2011**, *10*, 74.
[6] N. Yabuuchi, K. Kubota, M. Dahbi, S. Komaba, *Chem. Rev.* **2014**, *114*, 11636.
[7] Z. Lu, J. R. Dahn, *J. Electrochem. Soc.* **2001**, *148*, A1225.
[8] Z. Lu, R. A. Donaberger, J. R. Dahn, *Chem. Mater.* **2000**, *12*, 3583.
[9] J. M. Paulsen, R. A. Donaberger, J. R. Dahn, *Chem. Mater.* **2000**, *12*, 2257.
[10] W. Zuo, J. Qiu, X. Liu, F. Ren, H. Liu, H. He, C. Luo, J. Li, G. F. Ortiz, H. Duan, J. Liu, M.-S. Wang, Y. Li, R. Fu, Y. Yang, *Nat. Commun.* **2020**, *11*, 3544.
[11] M. Bianchini, J. Wang, R. J. Clément, B. Ouyang, P. Xiao, D. Kitchaev, T. Shi, Y. Zhang, Y. Wang, H. Kim, M. Zhang, J. Bai, F. Wang, W. Sun, G. Ceder, *Nat. Mater.* **2020**, *19*, 1088.
[12] Y. Lei, X. Li, L. Liu, G. Ceder, *Chem. Mater.* **2014**, *26*, 5288.
[13] M. Bianchini, J. Wang, R. Clément, G. Ceder, *Adv. Energy Mater.* **2018**, *8*, 1801446.
[14] Z.-Y. Li, J. Zhang, R. Gao, H. Zhang, Z. Hu, X. Liu, *ACS Appl. Mater. Interfaces* **2016**, *8*, 15439.
[15] D. H. Lee, J. Xu, Y. S. Meng, *Phys. Chem. Chem. Phys.* **2013**, *15*, 3304.
[16] P.-F. Wang, Y. You, Y.-X. Yin, Y.-S. Wang, L.-J. Wan, L. Gu, Y.-G. Guo, *Angew. Chem., Int. Ed.* **2016**, *55*, 7445.
[17] J. Xu, D. H. Lee, R. J. Clément, X. Yu, M. Leskes, A. J. Pell, G. Pintacuda, X.-Q. Yang, C. P. Grey, Y. S. Meng, *Chem. Mater.* **2014**, *26*, 1260.
[18] I. Hasa, S. Passerini, J. Hassoun, *J. Mater. Chem. A* **2017**, *5*, 4467.
[19] C. Ma, J. Alvarado, J. Xu, R. J. Clément, M. Kodur, W. Tong, C. P. Grey, Y. S. Meng, *J. Am. Chem. Soc.* **2017**, *139*, 4835.
[20] N. Yabuuchi, R. Hara, K. Kubota, J. Paulsen, S. Kumakura, S. Komaba, *J. Mater. Chem. A* **2014**, *2*, 16851.
[21] X. Chen, C. Cheng, M. Ding, Y. Xia, L.-Y. Chang, T.-S. Chan, H. Tang, N. Zhang, L. Zhang, *ACS Appl. Mater. Interfaces* **2020**, *12*, 43665.
[22] M. Zhang, D. A. Kitchaev, Z. Lebens-Higgins, J. Vinckeviciute, M. Zuba, P. J. Reeves, C. P. Grey, M. S. Whittingham, L. F. J. Piper, A. Van Der Ven, Y. S. Meng, *Nat. Rev. Mater.* **2022**, *7*, 522.
[23] U. Maitra, R. A. House, J. W. Somerville, N. Tapia-Ruiz, J. G. Lozano, N. Guerrini, R. Hao, K. Luo, L. Jin, M. A. Pérez-Osorio, F. Massel, D. M. Pickup, S. Ramos, X. Lu, D. E. McNally, A. V. Chadwick, F. Giustino, T. Schmitt, L. C. Duda, M. R. Roberts, P. G. Bruce, *Nat. Chem.* **2018**, *10*, 288.
[24] A. Ghosh, B. Senthilkumar, S. Ghosh, P. Amonpattaratkit, P. Senguttuvan, *J. Electrochem. Soc.* **2023**, *170*, 030538.
[25] L. Li, G. Su, C. Lu, X. Ma, L. Ma, H. Wang, Z. Cao, *Chem. Eng. J.* **2022**, *446*, 136923.
[26] T. Jin, P. Wang, Q. Wang, K. Zhu, T. Deng, J. Zhang, W. Zhang, X. Yang, L. Jiao, C. Wang, *Angew. Chem., Int. Ed.* **2020**, *59*, 14511.
[27] C. Zhao, Q. Wang, Z. Yao, J. Wang, B. Sánchez-Lengeling, F. Ding, X. Qi, Y. Lu, X. Bai, B. Li, H. Li, A. Aspuru-Guzik, X. Huang, C. Delmas, M. Wagemaker, L. Chen, Y.-S. Hu, *Science* **2020**, *370*, 708.
[28] V. Saïbi, L. Castro, I. Sugiyama, S. Belin, C. Delmas, M. Guignard, *Chem. Mater.* **2023**, *35*, 8540.
[29] K. Kubota, T. Asari, S. Komaba, *Adv. Mater.* **2023**, *35*, 2300714.
[30] P.-F. Wang, H.-R. Yao, X.-Y. Liu, Y.-X. Yin, J.-N. Zhang, Y. Wen, X. Yu, L. Gu, Y.-G. Guo, *Sci. Adv.* **2018**, *4*, aar6018.
[31] A. Gutierrez, W. M. Dose, O. Borkiewicz, F. Guo, M. Avdeev, S. Kim, T. T. Fister, Y. Ren, J. Bareño, C. S. Johnson, *J. Phys. Chem. C* **2018**, *122*, 23251.
[32] N. Yabuuchi, M. Kajiyama, J. Iwatate, H. Nishikawa, S. Hitomi, R. Okuyama, R. Usui, Y. Yamada, S. Komaba, *Nat. Mater.* **2012**, *11*, 512.
[33] X. Li, F. Bianchini, J. Wind, P. Vajeeston, D. Wragg, H. Fjellvåg, *J. Electrochem. Soc.* **2019**, *166*, A3830.
[34] M. A. Evstigneeva, V. B. Nalbandyan, A. A. Petrenko, B. S. Medvedev, A. A. Kataev, *Chem. Mater.* **2011**, *23*, 1174.

[35] R. A. House, U. Maitra, M. A. Pérez-Osorio, J. G. Lozano, L. Jin, J. W. Somerville, L. C. Duda, A. Nag, A. Walters, K.-J. Zhou, M. R. Roberts, P. G. Bruce, *Nature* **2020**, *577*, 502.
[36] M. Bianchini, A. Schiele, S. Schweidler, S. Sicolo, F. Fauth, E. Suard, S. Indris, A. Mazilkin, P. Nagel, S. Schuppler, M. Merz, P. Hartmann, T. Brezesinski, J. Janek, *Chem. Mater.* **2020**, *32*, 9211.
[37] M. Casas-Cabanas, M. Reynaud, J. Rikarte, P. Horbach, J. Rodríguez-Carvajal, *J. Appl. Crystallogr.* **2016**, *49*, 2259.
[38] R. D. Shannon, *Acta Cryst. A* **1976**, *32*, 751.
[39] F. Bianchini, H. Fjellvåg, P. Vajeeston, *J. Phys. Chem. C* **2019**, *123*, 4654.
[40] T. Matsunaga, H. Komatsu, K. Shimoda, T. Minato, M. Yonemura, T. Kamiyama, S. Kobayashi, T. Kato, T. Hirayama, Y. Ikuhara, H. Arai, Y. Ukyo, Y. Uchimoto, Z. Ogumi, *Chem. Mater.* **2016**, *28*, 4143.
[41] N. Yabuuchi, R. Hara, M. Kajiyama, K. Kubota, T. Ishigaki, A. Hoshikawa, S. Komaba, *Adv. Energy Mater.* **2014**, *4*, 1301453.
[42] K. Wang, P. Yan, M. Sui, *Nano Energy* **2018**, *54*, 148.
[43] Y. Xie, E. Gabriel, L. Fan, I. Hwang, X. Li, H. Zhu, Y. Ren, C. Sun, J. Pipkin, M. Dustin, M. Li, Z. Chen, E. Lee, H. Xiong, *Chem. Mater.* **2021**, *33*, 4445.
[44] S. Komaba, N. Yabuuchi, T. Nakayama, A. Ogata, T. Ishikawa, I. Nakai, *Inorg. Chem.* **2012**, *51*, 6211.
[45] D.-H. Seo, J. Lee, A. Urban, R. Malik, S. Kang, G. Ceder, *Nature Chem* **2016**, *8*, 692.
[46] J. W. Somerville, A. Sobkowiak, N. Tapia-Ruiz, J. Billaud, J. G. Lozano, R. A. House, L. C. Gallington, T. Ericsson, L. Häggström, M. R. Roberts, U. Maitra, P. G. Bruce, *Energy Environ. Sci.* **2019**, *12*, 2223.
[47] C. S. Yoon, D.-W. Jun, S.-T. Myung, Y.-K. Sun, *ACS Energy Lett.* **2017**, *2*, 1150.
[48] Y. Zhang, M. Wu, J. Ma, G. Wei, Y. Ling, R. Zhang, Y. Huang, *ACS Cent. Sci.* **2020**, *6*, 232.
[49] H. Hirsh, Y. Li, J.-H. Cheng, R. Shimizu, M. Zhang, E. Zhao, Y. S. Meng, *J. Electrochem. Soc.* **2021**, *168*, 040539.
[50] W. Zuo, F. Ren, Q. Li, X. Wu, F. Fang, X. Yu, H. Li, Y. Yang, *Nano Energy* **2020**, *78*, 105285.
[51] K. Dai, J. Mao, Z. Zhuo, Y. Feng, W. Mao, G. Ai, F. Pan, Y. Chuang, G. Liu, W. Yang, *Nano Energy* **2020**, *75*, 105285.
[52] P. Rapp, M. Xu, M. Bianchini, H. A. Gasteiger, **2024**, unpublished.
[53] E. N. Bassey, P. J. Reeves, M. A. Jones, J. Lee, I. D. Seymour, G. Cibin, C. P. Grey, *Chem. Mater.* **2021**, *33*, 4890.
[54] Y. Tang, Q. Zhang, W. Zuo, S. Zhou, G. Zeng, B. Zhang, H. Zhang, Z. Huang, L. Zheng, J. Xu, W. Yin, Y. Qiu, Y. Xiao, Q. Zhang, T. Zhao, H.-G. Liao, I. Hwang, C.-J. Sun, K. Amine, Q. Wang, Y. Sun, G.-L. Xu, L. Gu, Y. Qiao, S.-G. Sun, *Nat. Sustainable* **2024**, *7*, 348.
[55] J. Rodríguez-Carvajal, *Phys. B* **1993**, *192*, 55.
[56] H. M. Rietveld, *J. Appl. Crystallogr.* **1969**, *2*, 65.
[57] B. Ravel, M. Newville, *J. Synchrotron Rad* **2005**, *12*, 537.
[58] G. Kresse, J. Hafner, *Phys. Rev. B* **1993**, *47*, 558.
[59] G. Kresse, J. Furthmüller, *Comput. Mater. Sci.* **1996**, *6*, 15.
[60] G. Kresse, J. Furthmüller, *Phys. Rev. B* **1996**, *54*, 11169.
[61] G. Kresse, D. Joubert, *Phys. Rev. B* **1999**, *59*, 1758.
[62] J. P. Perdew, K. Burke, M. Ernzerhof, *Phys. Rev. Lett.* **1996**, *77*, 3865.
[63] S. Grimme, S. Ehrlich, L. Goerigk, *J. Comput. Chem* **2011**, *32*, 1456.
[64] S. Grimme, J. Antony, S. Ehrlich, H. Krieg, *J. Chem. Phys.* **2010**, *132*, 154104.
[65] A. Jain, G. Hautier, C. J. Moore, S. P. Ong, C. C. Fischer, T. Mueller, K. A. Persson, G. Ceder, *Comput. Mater. Sci.* **2011**, *50*, 2295.
[66] K. Okhotnikov, T. Charpentier, S. Cadars, *J. Cheminf.* **2016**, *8*, 17.
[67] S. P. Ong, W. D. Richards, A. Jain, G. Hautier, M. Kocher, S. Cholia, D. Gunter, V. L. Chevrier, K. A. Persson, G. Ceder, *Comput. Mater. Sci.* **2013**, *68*, 314.
[68] U. Herath, P. Tavadze, X. He, E. Bousquet, S. Singh, F. Muñoz, A. H. Romero, *Comput. Phys. Commun.* **2020**, *251*, 107080.